MILLIMETER-WAVE CHANNEL MEASUREMENTS IN AIRPORT ENVIRONMENT

by

Mahfuza Khatun

A dissertation

submitted in partial fulfillment

of the requirements for the degree of

Doctor of Philosophy in Electrical and Computer Engineering

Boise State University

May 2022

BOISE STATE UNIVERSITY GRADUATE COLLEGE

DEFENSE COMMITTEE AND FINAL READING APPROVALS

of the dissertation submitted by

Mahfuza Khatun

Dissertation Title: Millimeter-Wave Channel Measurements in Airport Environment

Date of Final Oral Examination: 7 March 2022

The following individuals read and discussed the dissertation submitted by student Mahfuza Khatun, and they evaluated the student's presentation and response to questions during the final oral examination. They found that the student passed the final oral examination.

Hani Mehrpouyan, Ph.D.	Chair, Supervisory Committee
Hao Chen, Ph.D.	Member, Supervisory Committee
Harish Subbaraman, Ph.D.	Member, Supervisory Committee
Hosseinali Jamal, Ph.D.	External Examiner

The final reading approval of the dissertation was granted by Hani Mehrpouyan,, Ph.D., Chair of the Supervisory Committee. The dissertation was approved by the Graduate College.

DEDICATION

To my father, who encouraged me to dream of higher education and inspired me to live a more meaningful life.

ACKNOWLEDGMENT

I want to thank several people for making my time as a graduate student at Boise State University memorable. First, I would like to express my heartfelt gratitude and admiration for my advisor Dr. Hani Mehrpouyan. His in-depth knowledge of wireless communication and excellent supervision has been an invaluable asset for me throughout my entire research life. Moreover, Dr. Mehrpouyan provided me with a perfect opportunity to work and collaborate with other brilliant researchers from the area of my Ph.D. research work. I appreciate the fact that, despite his hectic schedule, he always made time to answer my silly questions and provide me advice on how to solve the problem at hand, which helped to move the research forward. The goal of my dissertation would not have been achieved without his patience, motivation, excitement, and vast knowledge.

Besides, I would like to show my sincere appreciation to the rest of my committee members: Dr. Hao Chen and Dr. Harish Subbaraman, for their encouragement, insightful comments, and questions. All of them have been extremely helpful throughout my Ph.D. journey. They helped me a lot when I took graduate-level courses. I am thankful to them for their supervision and mentorship. I want to thank Dr. Subbaraman, in particular, for helping me to organize my research presentation. I am also grateful to Dr. Samia Islam for being my Graduate Faculty Representative. Next, I would like to acknowledge Dr. Hosseinali Jamal from Apple lnc. for being the

couragement in pursuing the highest degree, despite his Ph.D. research and our son Marwaan Mehdy's hectic schedule.

ABSTRACT

The wide spectrum available at millimeter-wave (mmWave) bands promises very high data rates and has been proposed as an attractive solution to provide high-speed and reliable wireless communication. Further, there are various potential usages of mmWave technology in transportation, aviation, autonomous vehicles, robotics, etc. Specifically, it is anticipated that automation through this technology will affect and improve the operations in every phase in airport environments. Consequently, the extended autonomous capabilities at airports will generate and consume more information and increase the demand for robust data transfer, which requires larger data rates than ever before. Hence, mmWave frequency, due to its large available spectrum, can be utilized for achieving such larger data rates, specifically for short-range applications. However, utilization of this technology crucially depends on precise measurement, characterization, parameterization, and modeling of the wireless channel. Moreover, our literature survey has revealed a pressing need for channel models for new airport applications of mmWave frequency band. Therefore, in this dissertation, we empirically characterize mmWave channels in a variety of settings for airport communication systems. Several measurement campaigns and environment descriptions at several bands (60, 73, and 81 GHz) are presented. A combination of line-of-sight and non-line-of-sight measurements were taken in both indoor and outdoor settings at the Boise airport. Some measurements at these high frequencies were captured at

Boise State University for comparison purposes. More specifically, we captured power delay profiles during the measurement campaign for the large-scale and small-scale fading analysis. For the large-scale fading effects, path loss models were computed from the power delay profiles at 60, 73, and 81 GHz, and some critical large-scale path loss parameters were extracted and analyzed. Moreover, we obtained mmWave outdoor small-scale fading statistics from 73 and 81 GHz channel measurement campaigns at Boise Airport. Wideband spatial fading measurements were made using a Gimbal attached with a linear track to move a receiver antenna for characterizing small-scale fading. Based upon our measurement data, we compared the receive signal amplitude with Rayleigh, Ricean, and log-normal fading models. In addition, we present the penetration, attenuation, and reflection characteristics of common building materials at these high-frequency bands. Measurements were taken for both wideband and narrowband signals to estimate attenuation at mmWave bands. These results are important to estimate coverage, interference analysis, and average error rate over a fading channel. Hence, they can aid researchers and system designers in the simulation and design of mmWave communication systems. Through extensive channel measurement campaigns and analysis, this dissertation contributes various insights to the field of wideband channel measurement and modeling in airport environments.

TABLE OF CONTENTS

LIST OF FIGURES

LIST OF TABLES

LIST OF ABBREVIATIONS

UAVs	Unmanned Aerial Vehicles
UAS	Unmanned Aircraft System
NASA	National Aeronautics and Space Administration
LOS	Line-of-sight
NLOS	None-line-of-sight
mmWave	Millimeter-Wave
TX	Transmitter
RX	Receiver
IF	Intermediate Frequency
LO	Local-Oscillator
RMS	Root Mean Square
PDP	Power Delay Profile
SSCM	Statistical Spatial Channel Model
CI	Close-in Free-space Reference Distance Model
FI	Floating-intercept Model
AWG	Arbitrary Waveform Generator
VSG	Vector Signal Generator
CDF	Cumulative distribution function
PTU	Pan-Tilt Unit
PDF	Probability distribution function
PA	Power Amplifier
LNA	Low Noise Amplifier
BPF	Band Pass Filter
ABG	alpha beta- gamma model
CIF	multifrequency CI model
USC	University of South Carolina
NCSU	North Carolina State University
MMSE	Minimum Mean Square Error
LS	Least Square Regression
V-V	Vertical-Vertical
ATM	Air traffic management systems

CHAPTER 1:

INTRODUCTION

This chapter introduces mmWave frequency bands and potential applications of these bands in aviation and airport communication systems.First, we'll go over a quick overview of wireless channels and why channel modeling is so important. Next, we explain the summary of contributions to the literature. Later, we conclude this chapter by stating the list of publications.

1.1 Introduction to Millimeter-wave Bands

In recent years, the growth of wireless devices and technologies has skyrocketed with various applications in cellular, vehicular, medical, and education. Simultaneously, every customer continues to demand greater and greater data rates in their devices, whereas the existing allocated spectrum does not provide enough bandwidth for carriers to increase the throughput for meeting this growing demand. To meet this demand, millimeter-wave frequency bands can be deployed to offer high data rates in wireless networks [20, 19, 24, 23]. The mmWave bands cover frequencies ranging from 30 GHz to 300 GHz. One essential enabling strategy for an excessive data rate increase is to utilize the unused raw mmWave spectrum. However, compared to sub 6 GHz signals, mmWave signaling suffers from more free space attenuation in the first meter of propagation. Rain attenuation adds a few dB to propagation path loss at

these high frequencies compared to free space. Nevertheless, a lossy mmWave channel could be made more reliable and efficient by leveraging highly directional steerable antenna structure and beam-forming techniques [20].

1.2   mmWave Airport Wireless Communications

As is well known, air travel, air transportation, and the usage of unmanned aircraft systems are burgeoning rapidly. An obvious consequence of the growth of passenger and freight air traffic and the future of Unmanned Aircraft System (UAS) into the worldwide airspace is continuously growing the air traffic density. Such increments in density means that safer operation will become more important as well as challenging. Therefore, today's communication systems for air-ground and airport surface systems may not have the throughput to maintain the same quality of service and security in the future. In light of this, the National Aeronautics and Space Administration (NASA) is funding research efforts to design and test new systems that will extend the throughput of the current air traffic management infrastructure. Furthermore, within the airport surface bounds, there are many organizations such as airlines, transportation and security groups, catering businesses, etc. Growth in the above-mentioned activities has coincided with a constant increase in the number of commercial and freight activities at airports. To ensure efficiency, safety, and security, these organizations' actions must be well-coordinated, and additional wireless devices will be required. Similarly, automation through the employment of machines and robots is expected to alter and improve airport operations in every way. As a result, the device's expanded autonomous capabilities will generate and consume more data, increasing the demand for reliable data transfer.

In the near future, unmanned aerial vehicles, unmanned aircraft systems, and

the associated operations are required to be handled at scale in conjunction with piloted airplanes in the airports and airspaces. Therefore, effective, efficient, and highly reliable wireless communication links are needed to support and meet these challenges. This, in turn, requires the use of the mmWave band spectrum in aviation technologies due to the availability of the wide spectrum at this band. This large bandwidth can be used to offer more exciting and new opportunities in such air transport and vehicular technologies. Making use of the large bandwidths in the mmWave bands such as the $60, 73$, and 81 GHz spectrum will help to achieve larger data rates, particularly for short-range applications in such a system.

1.3 Importance of Channel Measurements

In wireless communication technology, the medium where the signal travels, i.e., the channel, is a key element to successful signal transmission. In a terrestrial situation, a channel might be made up of several components that create various reflections, refraction, and diffraction of the transmitted signal, especially at high frequencies. Path loss, delay and phase shift, shadowing, noise, and interference pose problems to reliable signal transmission across a communication channel [3]. To fully utilize the potential of the spectrum in the mmWave band, understanding the propagation characteristics is an essential task to design and develop future mmWave communication systems. mmWAve channel modeling helps in determining a wireless channel affects the transmitted signal quantitatively. Hence, comprehensive knowledge of the channel models in indoor and outdoor settings is required to estimate the propagation characteristics at mmWave frequencies.

It is important to note that channel modeling helps in designing effective equalizers and beamforming techniques. Because correct knowledge of the signal strength of

various multipath components and the latency associated with each multipath component may be directly employed in receiver design, knowledge of channel characteristics helps to reduce system design costs. Furthermore, having an accurate channel model that offers knowledge of the environment can improve the effectiveness of channel coding.

As previously stated, channel characteristics in mmWave bands differ significantly from those in sub-6 GHz bands; because of the small wavelengths in these bands, diffraction is the weakest and least reliable propagation mechanism for mmWave communication systems. Furthermore, many little objects in the surroundings can be called scatterers, with a highly reflecting and scattering nature that results in feasible alternative links to the direct link [23]. Hence, a complete understanding of the channel characteristics requires raw channel data in different environments to characterize a mmWave channel accurately.

To this end, various teams at different organizations and universities have embarked upon channel measurement campaigns at mmWave frequencies. However, these various channel measurements have resulted in a variety of channel parameters for a similar propagation environment [20, 28]. Thus, this has required the need to collect more experimental propagation data from different environments, especially the airport environment, for developing more accurate and generalized models.

1.4   Summary of Contributions

One of the main goals is to evaluate future technologies for improving the safety and efficiency of air traffic management systems. Since airports are key components of ATMs, we investigate the deployment of new wireless systems at airports for various applications. To ensure the efficient deployment of such systems, a quantitative un-

derstanding of the wireless channels over which they operate is essential. Therefore, this dissertation mainly focuses on channel measurements at mmWave frequencies in different airport environment settings. According to the literature, our study is the first mmWave channel measurement research, which will provide the wireless research community with unique data on channel models for these high-frequency bands in airport environments. Specifically, this dissertation seeks to accumulate mmWave channel data at E-band frequencies ($70 - 90$ GHz) in an airport environment. The primary objectives and contributions of this dissertation are presented below:

In Chapter 3, we present large-scale path loss measurements and models at several mmWave bands—$60, 73$ and 81 GHz. The main contributions of this chapter are: 1) E-bands millimeter-wave propagation measurement campaigns were uniquely conducted within the indoor and outdoor environments at an airport setting. A large-scale measurement campaign was carried out at the Boise Airport terminal and tarmac. The close-in-reference and floating -intercept path loss models are carried out to extract the channel parameters based upon the collected data. 2) Our estimated path loss exponent describes coverage and link analysis, and estimated shadow factor presents signal fluctuations due to the obstacles caused by nearby environment. Hence, these channel parameters will be helpful for system coverage at mmWave frequencies in an airport environment.

We obtain 73 GHz and 81 GHz small-scale spatial fading measurements in Chapter 4. The main focuses of this chapter are 1) We recorded Power Delay Profiles for various angular directions for the wideband propagation measurements. To capture PDPs for the various angular direction, we utilized a linear track along with a gimbal at the receiver to move the directional horn antenna. More than 825 PDPs

were measured at each mmWave band in an outdoor airport and an indoor campus environment. 2) Moreover, these measurements present small-scale angular power profiles for both line-of-sight and non-line-of-sight scenarios. The statistical analysis of our small-scale fading measurements is unique for the setup in the airport areas. These results are potentially applicable to obtain amplitude gains for all other airports. 3)In addition, our data will help to estimate the average error rate for different transmission techniques over a fading wireless channel.

Chapter 5 represents penetration and reflection models of building materials in the campus environment. We collected power delay profiles in three different measurement campaigns at 60, 73, and 81 GHz channels. Our main contributions are 1)We performed penetration and reflection loss measurement campaigns at three buildings on the campus of Boise State University. The received signal strength was measured to test indoor and outdoor building materials such as clear glass, tinted glass, wood, and drywall. These results indicate that high-frequency reuse is needed between indoor and outdoor networks. These results will help to estimate the penetration and reflection characteristics of building materials at high-frequency bands. 2) Our contribution was to report attenuation test at 73 GHz in an indoor setting. Standard building materials, such as plywood, drywall, clear glass, brick, were tested for attenuation at this high frequency. 3) Moreover, indoor reflection characteristics of common building materials are carefully studied at 60,73 and 81 GHz using a narrow-band signal with directional horn antennas. To develop mmWave wireless systems, we need to know the penetration and reflection characteristics (refractive indexes) of various construction materials in millimeter-wave bands to evaluate indoor and outdoor multipath propagation characteristics at higher frequencies with multiple objects. Hence,

these results will help system designers to model a mmWave wireless link which is a significant contribution to the wireless community.

1.5 List of Publications

The publications resulting from the research reported in this dissertation are included in this section.

1.5.1 Conferences

1. M. Khatun, C. Guo, H. Mehrpouyan, "Penetration and Reflection Characteristics in Millimeter-Wave Indoor Channels" in ICEAA - IEEE APWC, 2021

2. C. Guo, M. Khatun, T. Berntson, H. Mehrpouyan, "Omnidirectional Small-Scale Fading Models in an Airport scenario in Millimeter-wave Frequency Bands: 73 and 81 Ghz", IEEE Veh. Technol. Conf. Fall, 2021.

3. M. Khatun, C. Guo, L. Moro, D. Matolak, and H. Mehrpouyan, "Millimeter-Wave Path Loss at 73 GHz in Indoor and Outdoor Airport Environments," in Proc. IEEE Veh. Technol. Conf. Fall, 2019.

4. M. Khatun, C. Guo, D. Matolak, and H. Mehrpouyan, "Indoor and Outdoor Penetration Loss Measurements at 73 and 81 GHz," in Proc. IEEE Global Commun. Conf., Dec. 2019.

5. M. Khatun, H. Mehrpouyan, and D. Matolak, "60 GHz millimeter-wave pathloss measurements in Boise Airport," IEEE Glob. Conf. on Signal and Inform. Process., pp. 1276–1280, 2018.

6. M. Khatun, H. Mehrpouyan, D. Matolak, and I. Guvenc, "Millimeter wave systems for airports and short-range aviation communications: A survey of

the current channel models at mmwave frequencies," IEEE Digital Avia. Syst. Conf., 2017.

1.5.2 Journals

1. M. Khatun, C. Guo, and H. Mehrpouyan, "Millimeter-Wave Directional Channel Measurements for Future 5G Wireless System in Airport Applications", submitted to IEEE access, 2021

2. N. Hosseini, M. Khatun, C. Guo, K. Du, O. Ozdemir, D. W. Matolak, I. Guvenc, H. Mehrpouyan, "Attenuation of Several Common Building Materials in Millimeter-Wave Frequency Bands: 28, 73 and 91 GHz", IEEE Antennas and Propagation Magazine, 2020

1.6 Dissertation Organization

This dissertation is organized as follows—in Chapter 3, path loss measurement campaigns are presented at the mmWave frequencies —60, 73, and 81 GHz. Chapter 4 presents small-scale fading and angular power profile measurements at 73 and 81 GHz. In Chapter 5, we investigate penetration, attenuation, and reflection loss measurements of several building materials in three different measurement campaigns. Chapter 6 concludes the dissertation with future work.

Notation: For the rest of this dissertation, the measurement data in each the chapter has been captured, extracted, and analyzed comprehensively and independently.

CHAPTER 2:

BACKGROUND

This dissertation seeks to embrace different channel measurements reported by other research groups in the mmWave bands. In that follows, we present a literature review of channel measurements and models at mmWave frequencies for various indoor and outdoor environments.

2.1   Indoor mmWave Channel Models

Many indoor mmWave research have been undertaken in recent years, mainly in the 60 GHz band, one of the most promising prospects for multi-gigabit wireless indoor communication systems. In addition, the wide available spectrum of the unlicensed $57 - 66$ GHz band is used in the current Wireless Gigabit Alliance (WiGig) WLAN and WirelessHD standards and devices for short-range applications [23, 5].

Using a directional horn antenna with 29 dBi of gain at the RX and an open-ended waveguide with 6.7 dBi of gain at the TX, Xu *et al.* investigated the indoor channel at 60 GHz [34, 35]. Results showed that LOS PLEs are lower than FSPL $(= 2)$ because reflections bounce off the grounds and ceiling. The resulting waveguide effect is attributed to increasing signal strength at the receiver. These results were similar to those obtained in indoor environments at sub-6 GHz frequency.

Smulders *et al.* carried out frequency-domain measurements in an indoor setting

for the 58 GHz channelt [29, 30, 31]. In the tiny room, the RMS delay spreads from the wideband mmWave experiments ranged from 15 ns to 45 ns. In larger rooms, this value varies between 30 ns and 70 ns, suggesting that more path with significant energy arrives at the receiver during a long time delay. There was also a worst-case RMS delay spread of 100 ns reported.

Little is known about other mmWave bands, aside from the majority of indoor propagation studies at 60 GHz. Haneda *et al.* [4, 18] used a VNA-based channel sounding structure to conduct several measurement campaigns in indoor shopping malls, train stations, and office environments in the 60 and 70 GHz bands.Research organizations are presently looking into the indoor propagation channel at mmWave frequencies other than 60 GHz. The $71 - 76$ GHz, $81 - 86$ GHz, and $92 - 95$ GHz bands have been suggested by the Federal Communications Commission for creating fixed point-to-point WLANs, and they will be deployed very soon. It's also worth noting that short-range applications use mmWave frequencies, notably E-band frequencies.

2.2 Outdoor mmWave Channel Models

Several investigations for outside channel measurements at mmWave frequencies have also been conducted. Rappaport in [24, 19, 20, 22] , for example, measured the channel at 28, 38, and 73 GHz in both LOS and NLOS scenarios in urban out-door environments.Large-scale properties at mmWave bands were the focus of these studies.Significant results from these channel measurements suggest that mmWave transmissions can be employed at distances of $100 - 200$ m, even in non-line-of-sight conditions. These channel measurements were taken in New York City, which is densely populated, and Austin, Texas, which is less densely populated [20]. In addition to that work, Rappaport *et al.* presented wideband small-scale fading mea-

surements for both directional and omnidirectional modeling at 73 GHz in an urban environment [32]. In most cases, both directional and omnidirectional LOS and NLOS recorded data follow the Ricean distribution well. In another work, Rappaport *et al.* conducted mmWave channel measurements for 28 GHz outdoor channels to study small-scale fading models [27]. Authors in [27] also observed that cumulative distribution function (CDF) of received signal amplitudes followed a Ricean distribution. Furthermore, authors in [25] performed small-scale fading measurements in industry and open-plan office environments. The mean amplitude of multipath components matched perfectly with log-normal distribution overall time bins.

Aside from work conducted by Rappaport, a channel measurement campaign was carried out in a lab environment for a 2.4 GHz channel [6]. Rayleigh, Ricean, and Two-Wave -Diffuse-Power (TWDP) distributions were investigated to fit the measured data. The Ricean distribution, in particular, was a far better fit for describing small-scale fading than the others [6]. At 81-86 GHz bands, Kyrö of Aalto University measured wideband channel in the street canyon and root-to-street scenarios [11, 12]. There was relatively minimal multipath delay spread in these investigations, and the actual and predicted delay spreads were extremely close. During their measurements campaign on the street, the authors [12] discovered that multipath exists in the E-band channel. However, their research did not go into thorough channel measurements for mobile or backhaul.

2.3   Reflection and Penetration Measurements

Few research has been done on the attenuation of various construction materials at mmWave frequencies. This attenuation is also known as "penetration loss," especially when propagating from outside to within (or vice-versa). In one notable work, at three

mmWave frequencies of 28, 73, and 140 GHz, the authors [33] investigated reflection loss, scattering, and the loss of partition structures (partition loss). As expected, the authors discovered more significant partition loss at higher frequencies than at lower frequencies. The material composition and antenna polarization can also have a significant impact on the degree of attenuation. These findings are restricted to clear glass and drywall construction materials.

Furthermore, at 28 GHz, the authors [36, 20] measured reflection and penetration loss of common building materials in dense metropolitan areas in New York City. They discovered that indoor-to-outdoor attenuation is greater than indoor-to-indoor and outdoor-to-outdoor propagation due to the building materials. mmWave signals can penetrate through a variety of inside materials and obtain powerful reflections from outdoor building materials, according to the findings. In addition, the authors [26] performed a 73 GHz penetration loss measurement for two antenna polarizations for different building materials. This study was conducted in a typical indoor office setting. Another study of propagation path loss in a building at 60 GHz was undertaken by the authors of [2]. According to these findings, the signal can be effectively confined to a single room because of the considerable penetration loss at this frequency. They also discovered that multipath components formed by reflectors inside a single room have extremely low RMS delay spreads.

From 3.5 to 24 GHz, the authors [14] conducted a penetration loss measurement campaign to investigate window penetration loss in a standard office structure. They selected a traditional office building, with reinforced concrete outside walls and double-glazed glass windows. They reported that as the receiver was moved farther into the building, the loss increased. The loss at 24 GHz was obtained lower than

that at 18 GHz at all defined places inside the building, while loss values at 6 GHz were found actually higher than those at 10 or 24 GHz. The glass window structure is reported as the cause of the difference among frequencies. This measurement can be thought of as a multi-material test that is difficult to generalize to different structures.

CHAPTER 3:

DIRECTIONAL PATH LOSS MEASUREMENT IN MILLIMETER-WAVE FREQUENCY BANDS: 60, 73 AND 81 GHZ

3.1   Introduction

At the Boise Airport, we provide experimental measurements for the 60, 73, and 81 GHz millimeter-wave bands. In both the indoor and outdoor environments at the Boise Airport, wideband propagation measurements were taken utilizing Keysight equipment with directional horn antennas at both the transmitter and receiver. On the taxiways and the airport tarmac, as well as inside the concourse gate areas, measurement campaigns were conducted that covered line-of-sight and non-line-of-sight scenarios. On the basis of directional power delay profiles, well-known directional large-scale path loss models are given and evaluated. Researchers may be able to use the information offered here to analyze and simulate the performance of next-generation mmWave wireless networks in an airport setting.

3.2   Equipment Description

Using wideband signal correlator-based channel sounder structure, we carried out path loss measurement campaigns. The hardware requirements for each campaign

are shown in detail in Table 3.1. Now, we present the 60, 73, and 81 GHz transmitter and receiver setup.

Table 3.1: Hardware Specifications of the 60, 73 **and** 81 **GHz Channel Measurements**

Campaign	60 GHz	73 GHz	81 GHz
Center frequency	60 GHz	73 GHz	81 GHz
IF frequency	5 GHz	4 GHz	3 GHz
LO frequency	2×10.205 GHz	2×38.5 GHz	2×39 GHz
Modulation scheme	BPSK		
Bandwidth	1.3 GHz	1.3 GHz	1.3 GHz
TX and RX antenna Type	Rectangular Horn Antenna		
TX antenna gain	25 dB	24 dBi	24 dBi
TX azimuth antenna HPBW	7.92∘	7∘	7∘
TX elevation antenna HPBW	9.65∘	11∘	11∘
RX antenna gain	25 dB	24 dBi	24 dBi
RX azimuth antenna HPBW	7.92∘	7∘	7∘
RX elevation antenna HPBW	9.65∘	11∘	11∘
Antenna polarization (TX-to-RX)	$V - V$		
Max transmit power	-5 dBm	6 dBm	3 dBm
Max measurable path loss	102 dBm	123 dBm	122 dBm

(a) Transmitter

Figure 3.1: Transmitter setup

3.2.1 73 and 81 GHz Setup

The block diagram for the transmitter is shown in Fig. 3.1. The baseband and IF signal source used in this work is an Arbitrary Waveform Generator. The signal is digitally modulated with binary phase-shift keying modulation. The modulated signal from the AWG is connected to two devices using two cables: one was connected to the mixer as the IF signal, and another part was connected to the scope as the reference signal. The mixer is used along with a local oscillator for further up-conversion at the desired frequency. The waveguide RF output signal is connected to a bandpass filter. To remove the undesirable sideband, a band-pass filter is utilized. Before connecting to the horn antenna, the filter's output is passed into a power amplifier.

DSA V084A — VDI Mixer — Low Noise Amplifier — Bandpass filter — Horn antenna

N5183A
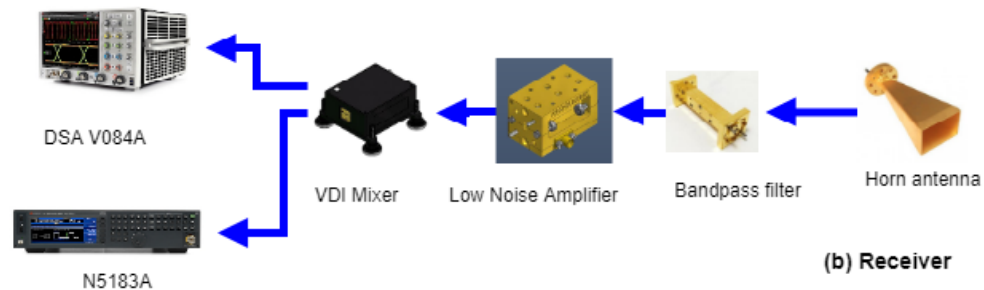
(b) Receiver

Figure 3.2: Receiver chain setup

The receiver chain is shown in Fig. 3.2. An identical horn antenna is used at the RX. The received signal from the antenna is amplified and undesirable out-of-band interference is removed using a low noise amplifier and a band-pass filter. The received signal is down-converted to a lower intermediate frequency using a mixer. The IF signal is then fed to the scope, where the power delay profiles are recorded for the post-processing. The channel data are recorded to a laptop for each measurement.

A 10 MHz clock signal and trigger pulse are used to connect and synchronize the transmitter and receiver.
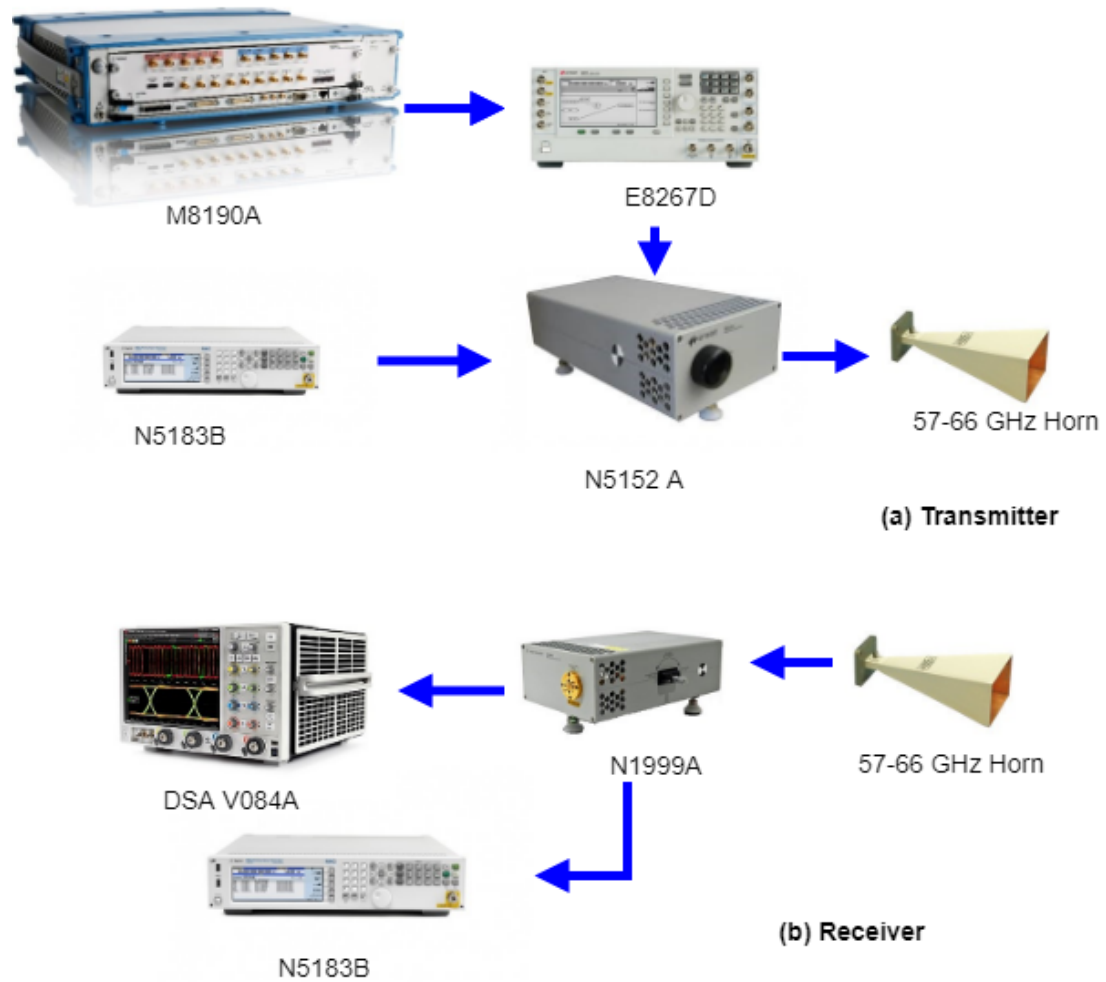
Figure 3.3: 60 GHz hardware setup

3.2.2   60 GHz Setup

The hardware setup is constructed through a combination of equipment that was purchased from Keysight. Fig. 3.3 shows the hardware setup constructed with several types of equipment: 1) an arbitrary waveform generator, a vector signal generator,

an up-converter, a down-converter, and two horn antennas. The embedded computer controller is connected to the Keysight M8190A AWG. The modulated signal is generated with 1.3 GHz bandwidth via the AWG. Subsequently, the Keysight E8267D VSG upconverts this signal to the intermediate frequency band at 5 GHz. This signal is further upconverted via the Keysight N5152A up-converter to 60 GHz. The up-converter uses a local oscillator that operates at 10.205 GHz. The 60 GHz RF signal from the mixer is fed to the transmitter horn antenna. On the receiver side, the same horn antenna is used. This antenna is connected to the input of the Keysight N1999A millimeter down-converter, and the LO for this mixer is set to 13.33 GHz in order to down-convert the signal to the IF of 5 GHz again. The received signal is finally fed to the Keysight DSAV084A scope, where the received power level is measured. The Keysight 89600 VSA software was used to capture the power measurements data. The gain of the horn antenna is 25 dB on both the transmitter and receiver sides with 7.92° half-power beamwidth. The rest of the parameters used for the measurement campaign are listed in Table 3.1.

3.3   Airport Measurements

The 73 and 81 GHz measurements were performed in both indoor and outdoor environments at the Boise Airport shown in Fig. 3.1 and 3.2. In the airport, the 60 GHz campaign was conducted in the gate and baggage areas for the LOS scenario. The airport is a medium-small size airport in Boise, Idaho. Measurements were made for both airport indoor and outdoor settings in LOS and NLOS scenarios.
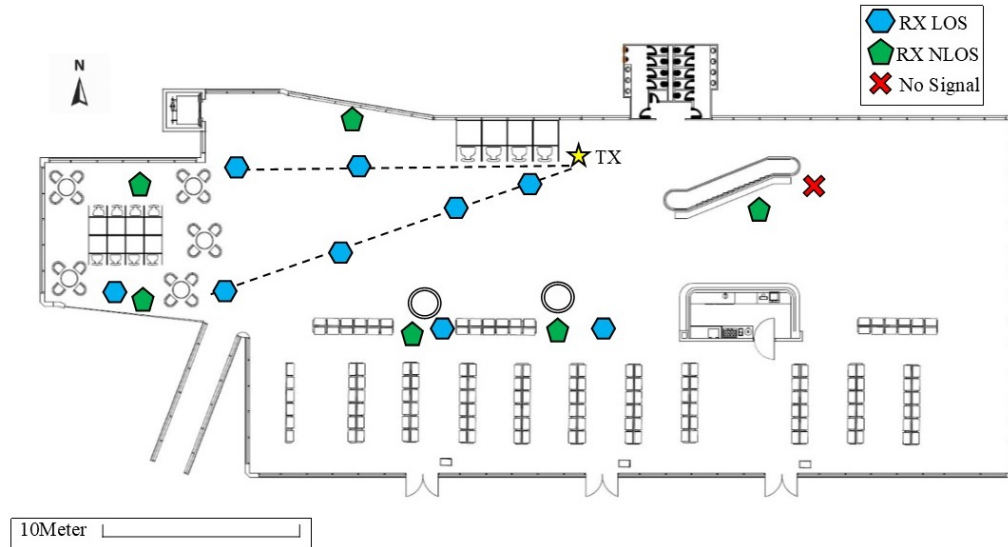
Figure 3.4: Floor plan of gated area in an indoor scenario at Boise Airport, showing transmitter and receiver locations.

3.3.1   Airport Indoor Environment

Indoor measurements were performed at the concourse C area in the airport terminal. Fig. 3.4 shows a concourse C area, which is a typical area in a small airport. There are 10 gates, one set of escalators, one gift shop, one coffee shop, restrooms, a waiting area containing about 250 seats, and an office-type cubical area. The Concourse C area has a carpet floor for a seating area and office type area, and ceramic floor for the rest. There are mineral fiber drop ceiling tiles above the carpet floor area and perforated metal ceiling tiles above the ceramic floor area. The southside of concourse C area uses clear glass to divide indoor and outdoor. The rest of the walls in this area are drywalls.

The 60 GHz indoor campaigns were conducted in the gate and baggage claim areas at the Boise Airport. Some indoor and outdoor environments are found in

Figure 3.5: Map of tarmac at Boise Airport, showing transmitter and receiver designated by doted lines.

Appendix C.

3.3.2 Airport Outdoor Environment

Fig. 3.5 shows the airport outdoor environment, which is located outside in between B and C gates. The measurement was performed near a boarding bridge, terminal building, a couple of pickup trucks, and, sometimes during measurement, an aircraft in the surrounding area. The ground is concrete, the same as a typical outdoor surface environment. The transmitter is placed next to the terminal building as well as the boarding bridge. During the measurements, there are truck and van impediments between the TX and the RX. Only a few trucks stand between the TX and the RX in an NLOS area with modest barriers, or the RX is immediately behind a truck or van corner.

3.4   Measurement Procedure

3.4.1   73 and 81 GHz

For indoor LOS scenarios, one TX and six RX locations were used in the measurements. At 73 GHz, the distance between TX and RX ranged up to 22 m in the indoor scenarios and up to 20 m in the outdoor scenarios at 73 GHz. The distance was measured with a laser meter and double-checked with a measuring tape, resulting in a distance accuracy of a few centimeters. To eliminate small-scale effects, the RX was moved in half-wavelength increments on an automated linear track of 400 mm at each position. At each track point, a power delay profile measurement was taken. For the measurement procedure, once the transmitter was configured to transmit, the receiver (carrying cart) was moved at the RX locations described in the prior subsection. For outdoor scenarios, the heights of the TX and RX antennas were set at 1.3 m and 1.2 m, respectively, from the ground level, and these values were set at 1.5 m and 1.2m for inside scenarios. All measurements were made in V-V polarization.

3.4.2   60 GHz

The measurements were done in the gate area environment at 60 GHz at 11 different places ranging from 1 meter to 20 meters with 2 meter increment steps. In both airport settings, the transmitter and receiver sides were structured with two moveable carts equipped with the equipment. The transmitter cart stayed fixed while the receiver cart was moved to different sites to collect data across various distances. Two antennas were kept in the point-point position at all times. It's critical that the measurements in the airport take place while the gate area is open. This allowed us to take into account the impact of human shadowing. Some pictures are found in

Table 3.2: 73 and 81 **GHz directional CI path loss models for LOS and NLOS environments at Boise airport**

Directional CI path loss with $d_o = 1$ m					
Frequency	Environment	LOS		NLOS	
		n	σ,dB	n	σ,dB
73 GHz	Indoor	2.05	2.34	3.56	3.47
	Outdoor	2.65	2.65	4.46	5.25
81 GHz	Indoor	2.52	3.32	3.82	5.42
	Outdoor	2.54	4.74	3.99	3.0

Appendix C.

3.5   Directional Path Loss Models

We developed path loss models based on our collected data from the airport environments for all three bands. Path loss models estimate the attenuation over a distance of propagating signals and are vital for designing communication systems. Different types such as deterministic, empirical, and stochastic of large-scale path loss models exist, but measurement-based path loss models provide realistic insight into propagation characteristics of a wireless channel. The relationship between propagation path loss and the TX-RX separation distance is based on both the antenna heights and obstructions between the transmitter and receiver. Along with knowledge of transmit power, received power P_r(dBm), can be expressed by: [21]

$$P_r(\text{dBm}) = P_t(\text{dBm}) + G_t(\text{dB}) + G_r(\text{dB}) - PL(\text{dB}), \tag{3.1}$$

where, P_t is the transmit power in dBm

G_t is the antenna gain of transmitter in dBi

and G_r is the antenna gain of receiver in dBi

PL is the path loss at distance d, in dB.

3.5.1 Close-in free space reference distance model

The *close-in* free space reference distance model [23, 21, 24] path loss model is usable in LOS and NLOS environments. It is developed based on the log-distance model. When a signal travels from one site to another for a particular TX-RX separation, each multipath may encounter different obstacles, resulting in varying levels of shadowing effect on the received signal. This phenomenon is called log-normal shadowing. This CI model is presented by (3.2):

$$PL_{CI}(d)[\text{dB}] = \text{FSPL}(f, d_0) + 10n \cdot \log_{10}(\frac{d}{d_0}) + \chi_\sigma, \quad \text{for} \quad d \geq d_0, \quad \text{where} \quad d_0 = 1\text{m},$$

$$(3.2)$$

where, n is the PLE, and χ_σ is a normal random variable with mean 0 dB and standard variation σ in dB. Howerver, σ is also known as shadow factor due to large-scale channel fluctuations in the wireless channel [21]. The CI model employs a physically-based reference distance d_0, and the close-in free space path loss in dB, $\text{FSPL}(f, d_0)$ is given by (3.3):

$$\text{FSPL}(f, d_0) = 20 \log_{10} \frac{4\pi d_0}{\lambda}, \tag{3.3}$$

The PLE, n can be determined by using MMSE that fits the measured data with the smallest error (by minimizing σ) overall measurements from a particular measurement campaign. For the CI model, the researcher proposed $d_o = 1$ m as

a standard in [24, 17]. For high gain directional antennas, the far-field radiation patterns (Fraunhofer distance) can be obtained at a distance greater than 1 m from the antenna. Hence, standardizing a reference distance at 1m provides us to compare a model between different frequency bands and measurements reported from other researchers and authors. It also allows closed-form computation in analysis, and intuitive computation of received power without a calculator since the power decays by 10n dB per decade of distance beyond 1 m [24].

3.5.2 Floating intercept path loss model

The *floating-intercept*, is introduced in [16]. This model has no physical reference, but it fits the best line to the measurement data with the least square regression. The FI model is used in the WINNER II and 3GPP standards [1, 10]. Unlike the CI model, the FI model does not consider a physically-based anchor to the transmit power and presented by (3.4):

$$PL_{FI}(d)[\text{dB}] = \alpha + 10.\beta \log_{10}(d) + \chi_\sigma, \qquad (3.4)$$

where, α is the floating intercept in dB,

β is the linear slope, χ_σ is a normal random variable with standard variation σ, which describes large-scale signal fluctuations about the mean path loss over distance. The LS regression approach creates a line-of-best fit to the empirical data to solve α and β for minimizing σ [23, 16].
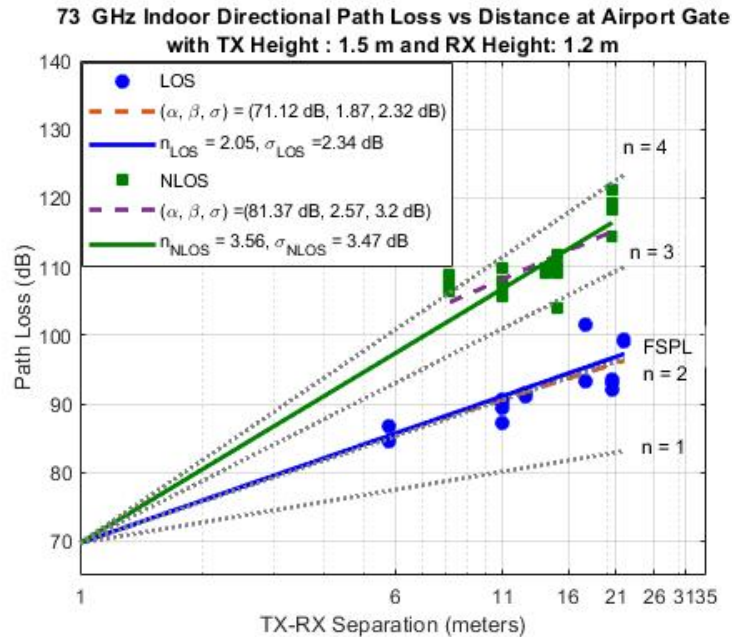
Figure 3.6: 73 **GHz indoor CI** ($d_o = 1$ **m) and FI path loss models in an airport gated area. Each blue circle represents LOS path loss values, green squares represent obstructed NLOS path loss values.**

3.6   Results analysis

In this section, we present and analyze path loss results for three mmWave channels—60, 73, and 81 GHz. We carried out the close-in free space reference distance and floating intercept models based upon our measurement data. These models are widely used for mmWave channel measurement in recent studies [24, 20, 15].

3.6.1   73 and 81 GHz Path loss

Table 3.2 shows the directional CI path loss parameters, with $d_o = 1$ m estimated from (3.2) for the airport indoor and outdoor environments at 73 and 81 mmWave bands. The 73 GHz, LOS PLE for the airport indoor and outdoor scenarios, are 2.05 and 2.65, respectively. The 73 GHz, LOS PLE for the indoor environment, is
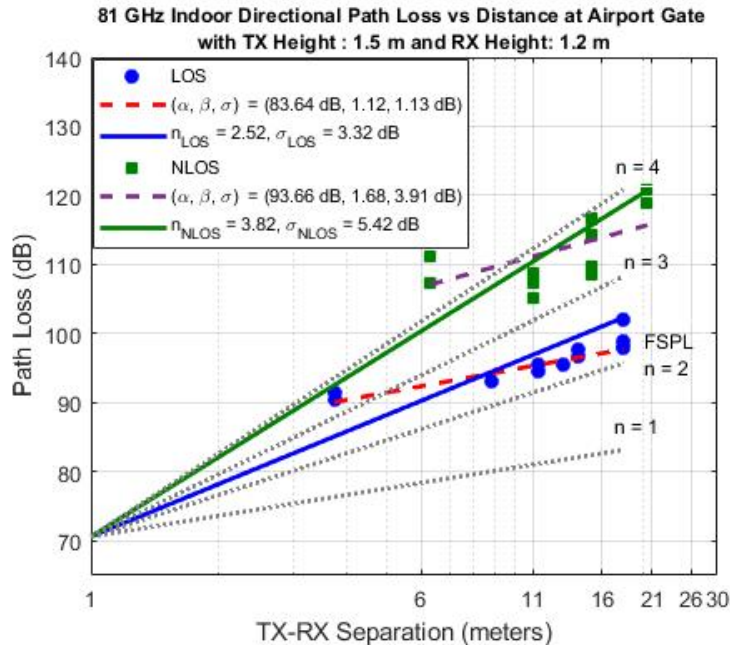
Figure 3.7: 81 **GHz indoor CI** ($d_o = 1$ **m) and FI path loss models in an airport gated area. Each blue circle represents LOS path loss values, green squares represent obstructed NLOS path loss values.**

close to the FSPL ($= 2$) due to constructive interference, and the shadow factor standard deviation for the indoor and outdoor measurements is approximately 3 dB. As the LOS PLE being approximately $n = 2.5$ for almost all scenarios for 73 and 81 GHz channels, this indicates the sensitivity of beam pointing in future mmWave wireless systems. To improve LOS field measurements, we used laser pointers to ensure boresight alignment.

The 81 GHz, NLOS CI model, shows a much larger shadowing that is approximately 5 dB for the airport indoor environment, indicating much larger fluctuations in received signal strength around the mean received power over all TX-RX separation distances. This is most likely due to the obstacles caused nearby environment, which made the channel more fluctuated.
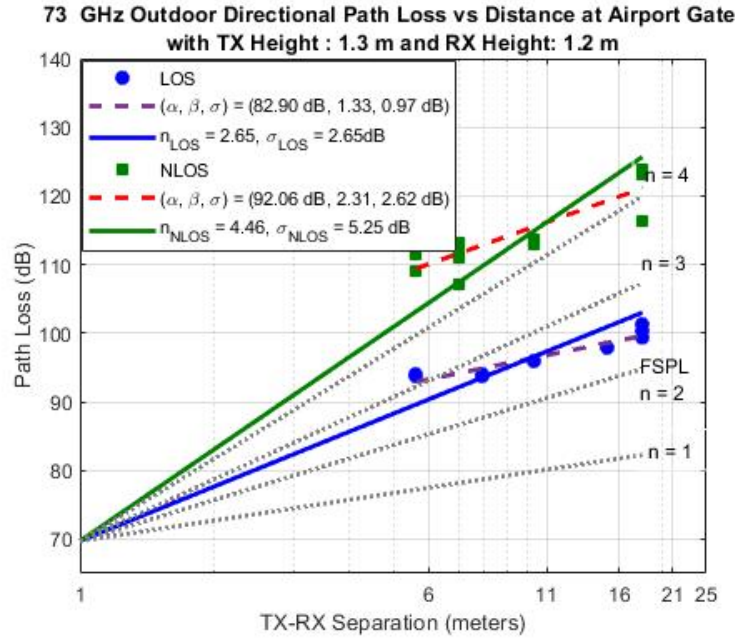
Figure 3.8: 73 **GHz outdoor CI** $(d_o = 1$ **m) and FI path loss models in an airport tarmac area. Each blue circle represents LOS path loss values, green squares represent obstructed NLOS path loss values.**

Table 3.3: 73 **and** 81 **GHz directional FI path loss models for LOS and NLOS environments at Boise airport**

Directional FI path loss model							
Frequency	Environment	LOS			NLOS		
		α,dB	β	σ, dB	α,dB	β	σ,dB
73	Indoor	71.12	1.87	2.32	81.37	2.57	3.2
	Outdoor	82.90	1.33	0.97	92.06	2.31	2.62
81	Indoor	83.64	1.12	1.13	93.66	1.68	3.91
	Outdoor	85.98	1.12	1.09	83.69	2.80	2.74

Table 3.3 shows estimated parameters for the FI model from (3.4), where it can be seen that path loss value (α) can vary widely (approximately 10 dB) compared to free space path loss at 1 m for the LOS 73 GHz and 81 GHz channels. The LOS value, α was obtained at 71.12 dB and 82.90 dB for the airport indoor and outdoor scenarios, respectively, compared to 69.7 dB theoretical FSPL at 1 m at 73 GHz. The 81 GHz
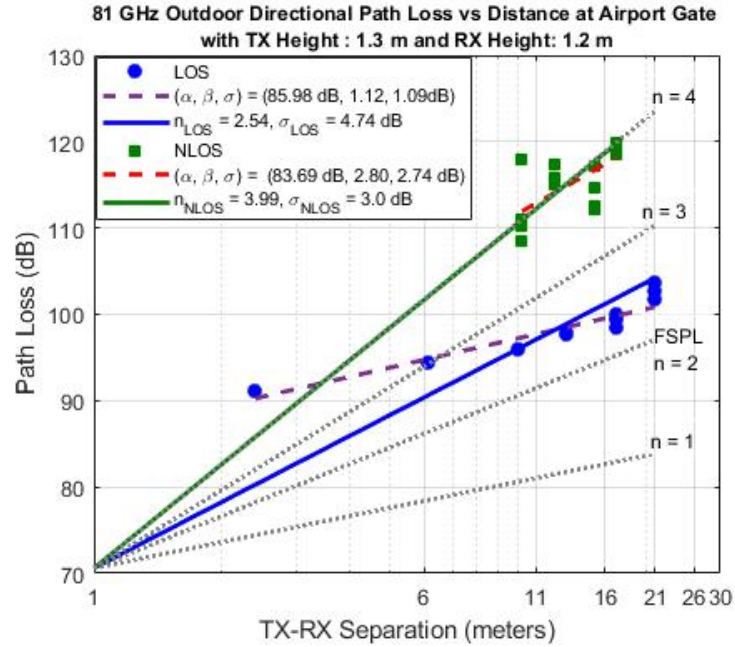
Figure 3.9: 81 **GHz outdoor CI** ($d_o = 1$ **m**) **and FI path loss models in an airport tarmac area. Each blue circle represents LOS path loss values, green squares represent obstructed NLOS path loss values.**

LOS values are extracted at 83.64 and 85.98 dB as compared to the theoretical FSPL (70.6) in indoor and outdoor environments, respectively. This shows that the FI model lacks a physical link to the transmitted signal power, and does not physically model what actually happens in a practical LOS system.

Figs. 3.6 and 3.7 display the CI ($d_0 = 1m$) and FI directional path loss models, and scatter plots at 73 GHz and 81 GHz for LOS and NLOS airport indoor environments. The strength of the CI model compared to the FI model is that it only requires a single parameter to accurately predict path loss. The FSPL line provides an accurate physically-based reference anchor point for estimating LOS path loss.

The 73 GHz and 81 GHz NLOS CI model standard deviations are within 1.5 dB of the respective NLOS FI models. The 81 GHz LOS slope value is obtained at
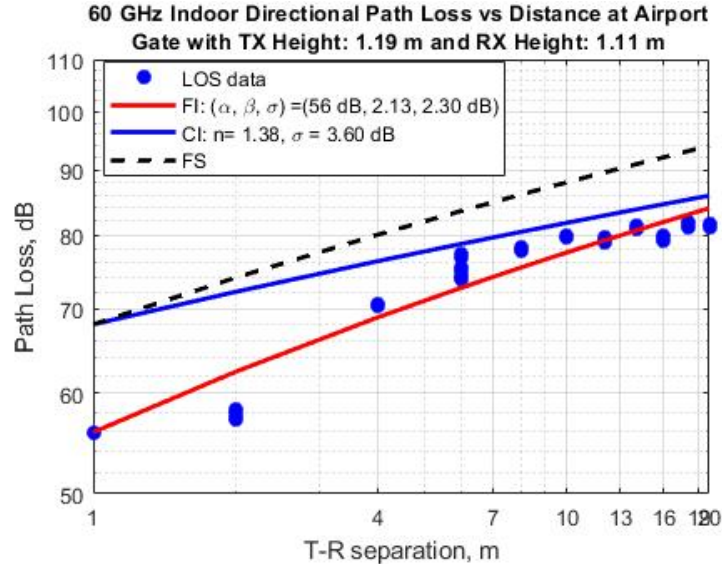
Figure 3.10: 60 **GHz indoor CI** ($d_o = 1$ m) **and FI path loss models in an airport gate area. Each blue circle represents LOS path loss values. Black dashed, blue solid and red solid lines represent FSPL, CI and FI fitted lines.**

$\beta = 1.12$ estimated from the FI model, which indicates a channel with extremely low loss, showing the lack of fundamental physics in the FI model.

Figs. 3.8 and 3.9 shows the corresponding scatter plots for the airport outdoor environments at 73 GHz and 81 GHz. The 73 outdoor LOS PLE (2.65) is slightly greater than 2.0, which is most likely due to antenna alignment in hot sunny weather during measurements. In addition, the NLOS PLE is slightly larger for airport outdoor environments than airport indoor for both E-band channels, which may be ascribed to more strong reflected paths in these environments.

3.6.2   60 GHz Path Loss

Figs. 3.10 and 3.11 show the scattered measurement data along with the CI and FI for airport scenarios. The PLE value ($n = 2.13$) is slightly more than the free
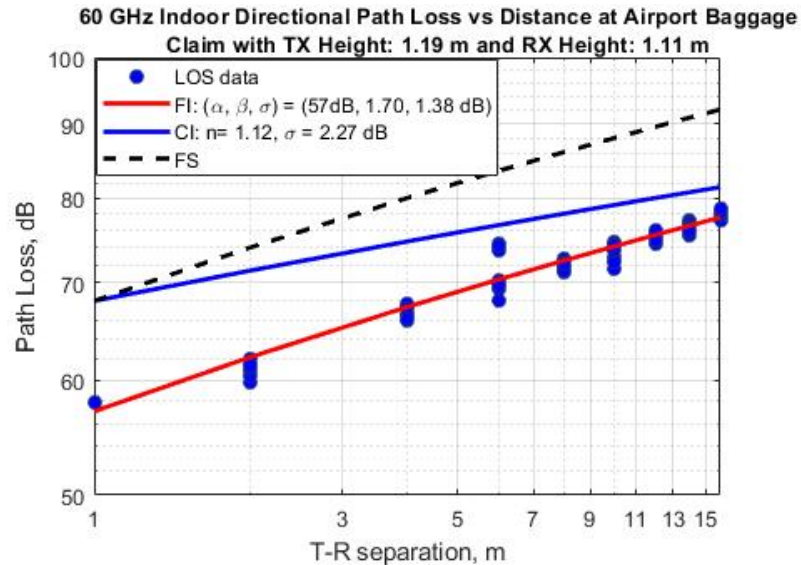
Figure 3.11: 60 **GHz indoor CI** ($d_o = 1$ m) **and FI path loss models in an airport baggage claim area. Each blue circle represents LOS path loss values. Black dashed, blue solid and red solid lines represent FSPL, CI and FI fitted lines.**

space value in the airport gate area in the FI approach due to the loitering of the passengers in this area during the measurement time. The LOS FI PLE for the airport gated and baggage areas are measured 2.13 and 1.70, respectively. The PLE for the baggage claim areas is slightly better than free-space propagation (n =2). This may be attributed by the waveguiding effect, where the multipath components are guided along the hallways, and constructive interference is created at the RX antenna. The CI model overshoots the data in plots because this model depends on the free space values. It is found that the CI model is close to the FSPL and FL model fits best with the data.

The standard deviations for the shadowing terms are also enlisted in Table 3.4. The shadowing explains the random variation of the path loss model. It is important

Table 3.4: 60 **GHz path loss parameters at Boise Airport**

60 GHz Directional Path Loss Models								
Environments	Scenarios	TX antenna height, m	RX antenna height, m	CI		FI		
				n	σ, dB	α, dB	β	σ,dB
airport gate	LOS	1.17	1.13	1.38	3.60	56	2.13	2.30
airport baggage	LOS	1.19	1.11	1.12	2.27	57	1.70	1.38

to know the shadowing effects for the ranges of the path loss values. The shadow factor is higher in LOS gated areas than baggage claim areas. The FI and CI model estimated shadow factor 2.30 dB and 3.60 dB, respectively. Since the airport gate environments are more spacious than an office room and hallway, wave scattering could be very rich in this case, and also it has many metallic chairs compared to the hallway and small room environments. This causes higher path loss values at airport gated areas than in other indoor environments.

3.7   Conclusion and Summary

In this chapter, we derive path loss models from extensive mmWave indoor and outdoor propagation measurements using directional horn antennas at 60, 73 GHz, and 81 GHz in the Boise Airport. Directional path loss models are presented, yielding insight into mmWave propagation characteristics in indoor and outdoor environments. We used close-in reference distance and floating-intercept path loss models to estimate the path loss exponent and shadow factor. Our work shows that the CI PLEs are close to the theoretical PLE (= 2) of the free-space model, whereas the FI gives a better fit to the measured data. The FI NLOS standard deviation (σ) is more at both 73 and 81 GHz channels in the airport indoor environment than the airport outdoor environment. The airport indoor environment had more obstacles (i.e., chairs, walls, elevator, and partitions), which create more reflective nature in an indoor scenario.

These results also show that the indoor airport environment is uniquely different from other indoor settings due to its large and open nature.

CHAPTER 4:

OMNIDIRECTIONAL SMALL-SCALE FADING

MODELS AT MILLIMETER-WAVE

FREQUENCY BANDS: 73 AND 81 GHZ

4.1   Introduction

This chapter presents the omnidirectional small-scale fading measurements and analysis at millimeter-wave frequency bands —73 and 81 GHz —at the Boise Airport and Boise State University. Measurements yielded small-scale omnidirectional models and angular power profiles for line-of-sight and non-line-of-sight scenarios. Various angular combinations of PDPs were obtained by controlling the beam directions of the transmitter and receiver antennas using a gimbal. A linear track was employed at each receiver to move the antenna in half-wavelength increments.

4.2   Measurement Hardware Setup

The measurement setup for small-scale spatial measurement is an extension to the setup we present in Chapter 3.A wideband signal correlation time-domain channel sounding approach was employed for the wideband measurements. A chirp signal was generated in AWG for the wideband measurements. Detailed hardware parameters are provided in Table 4.1 For the small-scale fading measurements, we added a Gimbal

both on the TX and RX antenna for precise antenna pointing angles. This Gimbal is known as Pan-Tilt Unit, and the setup of this unit can be explained in Appendix B.

Table 4.1: Hardware Specifications for Small-scale Fading Measurement Campaign

Center Frequency,GHz	73	81
LO Frequency, GHz	2 x 38.5	2 x 39
IF Frequency,GHz	4GHz	3
Wideband Signal	Radar Chirp Pulse	Radar Chirp Pulse
Bandwidth, MHz	500	500
Antenna	Rectangular Horn Antenna	Rectangular Horn Antenna
Antenna Gain, dBi	24	24
3 dB beamwidth in azimuth plane,∘	7	7
3 dB beamwidth in elevation , ∘	11	11
Antenna Polarization	V-V	V-V
Max. transmit power	-5dBm	-4dBm

4.3   Measurement Environment and Procedure

The propagation campaign with frequencies of 73 and 81 GHz was completed in Boise, Idaho. The bandwidth of 500 MHz for arbitrary waveforms was implemented to study the wave propagation of 5G mmWave channels.

4.3.1   Gimbal Setup

The FLIR gimbal illustrated in Fig. 4.1 was used to correctly control and reproduce angles for each measurement point. Both the TX and RX antennas were attached to the top platform of their own individual gimbals; this will be referred to as TX and RX modules in each measurement campaign. The TX module was attached to the top of a tripod, while the RX module was attached to a linear track. The FLIR gimbal is able to rotate in both the azimuth and elevation angles. The azimuth angle was employed as the key adjustable feature to view the small-scale propagation fluctuations during this campaign. FLIR was specked to have the ability to fully rotate 360° from −180°

Figure 4.1: TX gimbal module with gimbal attached to TX antenna and tripod

to 180°, a maximum angle of −160° to 160° was chosen to allow for equally spaced

angle measurement steps. Two different ranges of angle adjustments were measured

for small-scale measurements. For 360° measurements, the goal was to model the angular spread while a range of −30° to 30° measurements were simply used to take directional measurements. To measure angular spread, the TX antenna was set to an angle of 0° and the RX antenna was placed in front of the TX. Measuring the half-power peaks of the TX peak power beam was then done by rotating the RX by the 360° and taking PDP measurements every 10°.

4.3.2 Outdoor Measurements

The PDP measurements were taken for both LOS and NLOS scenarios at the Boise Airport on the airport apron in December 2020. This outdoor environment is similar to the airport outdoor environment described in [9]. This channel is of interest to provide little known information on actively used apron areas for 5G wireless channels. TX and RX antenna separations of 7.4 m and 10 m were employed to perform LOS small-scale observations of the apron channel. The TX antenna was positioned on a tripod around 1.47 m from the ground in both outdoor and indoor cases. The RX antenna was placed on a linear track also 1.47 m from the ground. The configuration at which the antennas faced each other is considered to be at 0° azimuth and 0° elevation angles in this campaign. The TX antenna would remain static at 0° in the azimuth plane, while the RX antenna would be mechanically adjusted from −160° to 160° in the azimuth plane. Furthermore, this TX and RX procedure was used for NLOS measurements at an antenna separation of 8.5 m. Fig. 4.2 shows the relative TX and RX locations of the LOS and NLOS measurements. The RX was then adjusted $\lambda/2$ step across the linear track between each of the full rotation measurements for five steps.
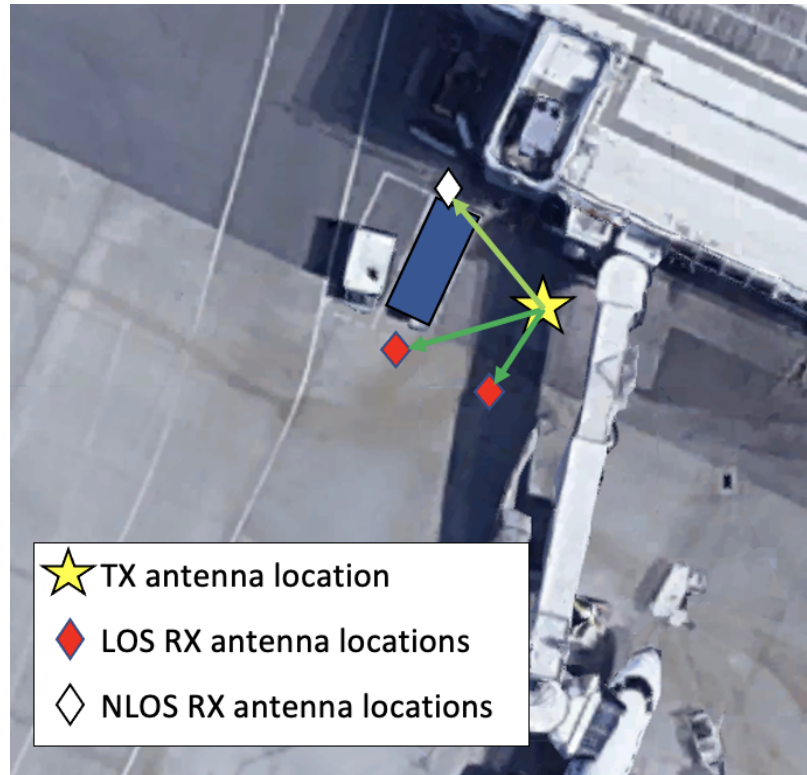
Figure 4.2: Overhead view of Boise Airport antenna locations

4.3.3 Indoor Measurements

Small scale measurements were completed in October 2020 at Boise State University on the 2nd floor of the Micron Engineering Center. This indoor environment is similar to the Boise State hallway environment described in [8]. A $32X2.2X1.9$ m^3 sized hallway was utilized as the channel environment. The infrastructure of the building walls was comprised of sheetrock with metal studs. The location chosen for the indoor measurements included one side of the hallway containing a sheetrock wall and the opposing side of the hallway containing office cubicles. The office cubicles were made of metal brackets, fabric, and wood with a mixture of wood, metal, and laminate desks. The ceiling was comprised of fiberboard material and the flooring was made of

concrete. This channel was chosen to mimic a common public channel environment for 5G wireless networks. The small-scale measurements for the indoor environment were done by capturing the LOS PDPs. To do this, the TX and RX antennas were separated by 3.9 m. The TX antenna remained static at $0°$ while the RX antenna was mechanically adjusted from $-160°$ to $160°$. Between each full rotation within a respective azimuth range, the RX module was adjusted $\lambda/2$ step across the linear track for five rotational sets.

4.4 Data Post Processing

The measured power delay profiles were recorded for the post-processing step. The maximum estimated noise level from all available power delay profiles was considered. To reduce the effect of noise, a threshold of 15 dB below the maximum peak was applied to each PDP so that it excludes random noise spikes. The directional measurements for multiple combinations of TX and RX angles were utilized. The approximated omnidirectional received power was synthesized from the directional received power for unique angle combinations in each TX-RX location combination [24]. Afterward, the amplitude of the received signal was determined. The square root of the total power in linear scale for all TX and RX antenna angle combinations was taken to obtain received signal amplitude. The received power at each angular combination was also utilized for depicting the angular power profile for every TX and RX location.

4.5 Omnidirectional Small-scale Fading Models

The Rayleigh distribution is the most widely utilized distribution function for statistical modeling of received signal amplitude. Rayleigh distribution characterizes

a scenario where many arriving multipath components have comparable delays and amplitudes. Rayleigh's probability density function for the amplitude a is expressed [3] in (4.1),

$$f_A(a) = \frac{a}{\sigma^2} e^{-\frac{a^2}{2\sigma^2}} \tag{4.1}$$

where σ is the standard deviation of the multipath component amplitudes. The Ricean distribution characterizes the presence of a strong dominant LOS path of the channel, and is described by (4.2),

$$f_A(a) = \frac{a}{\sigma^2} e^{-\frac{a^2 + v^2}{2\sigma^2}} I_o(\frac{av}{\sigma^2}) \tag{4.2}$$

where σ^2 is the variance of the multipath component amplitudes, v is the amplitude of the dominant path, and $I_o()$ is a modified Bessel function of the first kind and zero-order. The parameter K is the ratio of the amplitude of the dominant path and the all other path amplitudes and is described as by (4.3),

$$K = \frac{v^2}{2\sigma^2} \tag{4.3}$$

The probability density function of a log-normal distribution is given by (4.4),

$$f_A(a) = \frac{1}{\sqrt{2\pi}\sigma a} e^{-\frac{(loga - \mu)^2}{2\sigma^2}} \tag{4.4}$$

The mean and standard deviation of the path amplitudes are *mu* and *sigma*, re-

spectively. We compare the CDF of the measured received signal amplitude with Rayleigh, Ricean with a K-factor, and zero-mean log-normal distribution with standard deviation obtained from measured data.
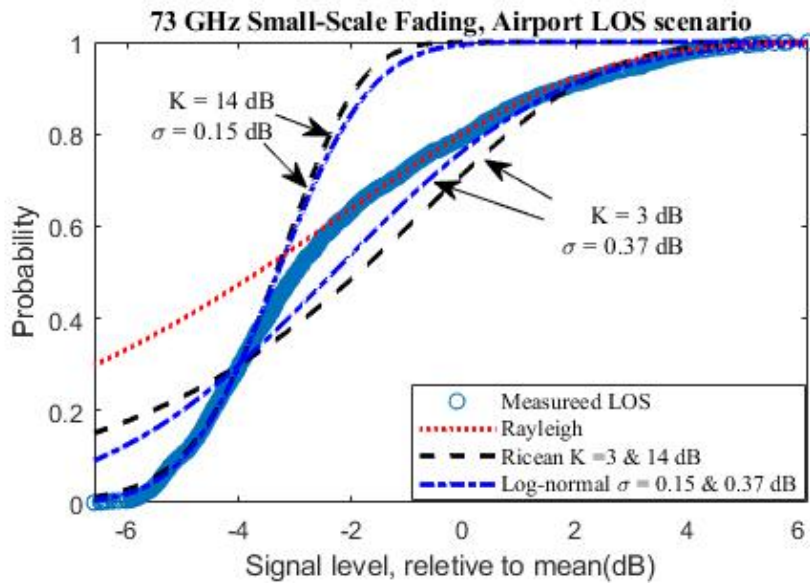
Figure 4.3: CDF of the measured 73 GHz small-scale fading of the received signal for the omnidirectional RX antenna pattern in the Airport LOS environment.

4.6   Result Analysis

4.6.1   Analysis of Small-scale Fading at 73 GHz

Figs. 4.3 and 4.4 show the CDF of the measured received signal amplitude, relative to the mean for the 73 GHz channel in the airport LOS and NLOS environments, respectively. In Figs. 4.3 and 4.4,the Rayleigh distribution is poorly fitted when compared to the measured 73 GHz small scale fading in both LOS and NLOS scenarios. Comparatively, log-normal and Ricean distributions are a closer fit to each other with the measured data. The measured CDF is bounded by Ricean distribution of K-factor
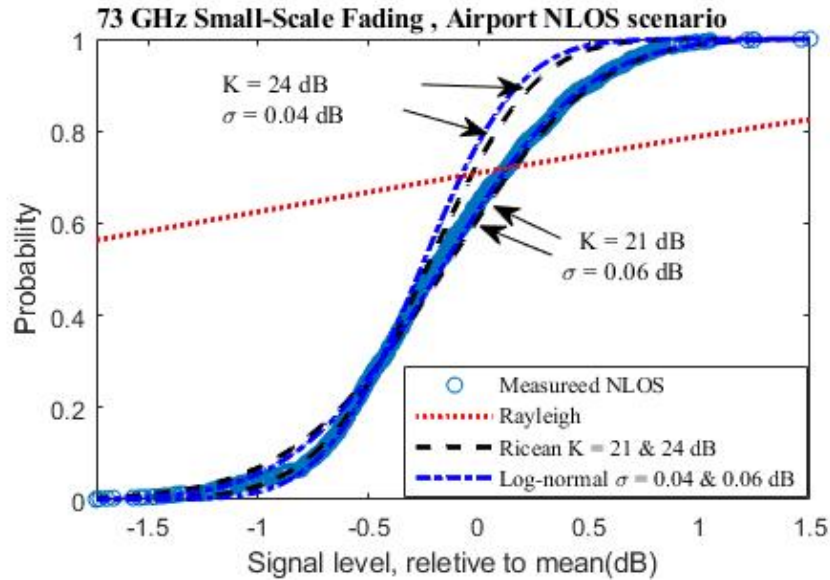
Figure 4.4: CDF of the measured 73 GHz small-scale fading of the received signal for the omnidirectional RX antenna pattern in the Airport NLOS environment
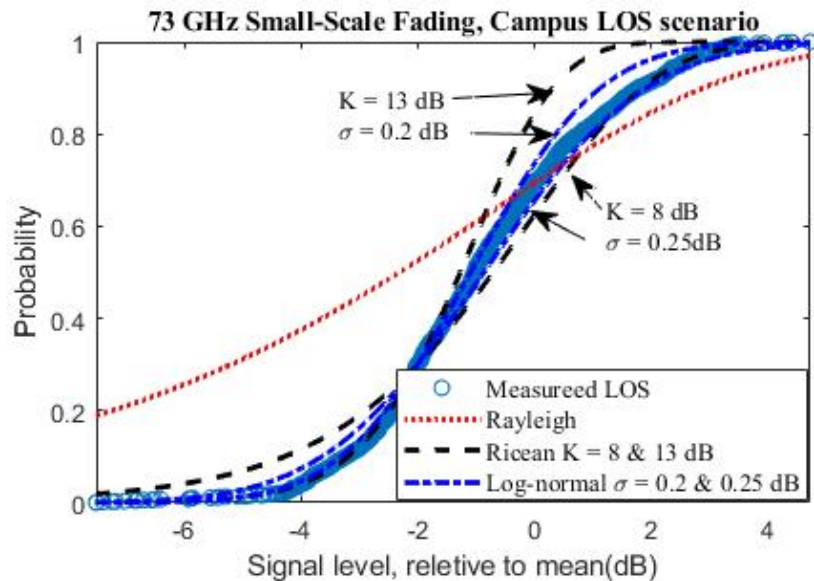
Figure 4.5: CDF of the measured 73 GHz small-scale fading of the received signal for the omnidirectional RX antenna pattern in the campus LOS environment.

ranging from 3 to 14 dB, and log-normal distribution with $\sigma = 0.15$ dB and 0.37 dB for the 73 GHz LOS channel as indicated in Fig. 4.3. As evident from Fig. 4.4, the measured NLOS small-scale fading curve matches well to both the Ricean and the log-normal distribution. However, the Ricean with $K = 24$ dB and the log-normal with $\sigma = 0.04$ dB fits the measured data in the tail region around -1.5 dB to -0.5 dB of relative signal level as shown in Fig. 4.4. Note that one detectable signal among all angular combination PDPs from the NLOS scenario in the outdoor airport environment had been found. The reason for a low σ and a high peak to the average of the path amplitude is caused by only one set of path amplitudes, which is above the noise floor.

Fig. 4.5 depicts 73 GHz small-scale fading in the indoor LOS environment for the omnidirectional model. The measured LOS curve is bounded by both the Ricean with $K = 8$ to 13 dB and log-normal with $\sigma = 0.25$ to 0.2 dB. The data fit well with the Ricean distribution in almost all scenarios because the strong dominant path has appeared in the measurement scenario, and for the NLOS measurements, most of the paths are strong because we avoided most of the paths due to the undetectable signals. It can be seen that the Rayleigh distribution fades are deeper. This is most likely due to a strong LOS path in an indoor environment.

4.6.2   Analysis of small-Scale Fading at 81 GHz

The CDFs for the 81 GHz small scale fading channel in airport LOS and NLOS environments are shown in Figs. 4.6 and 4.7. The CDF of received signal amplitudes are Ricean and log-normally distributed for both LOS and NLOS conditions. The measured data is Ricean distributed with K-factor ranging from $3-13$ dB, and $21-27$ dB in LOS (Fig. 4.6) and NLOS (Fig. 4.7) scenarios for an outdoor airport environment,
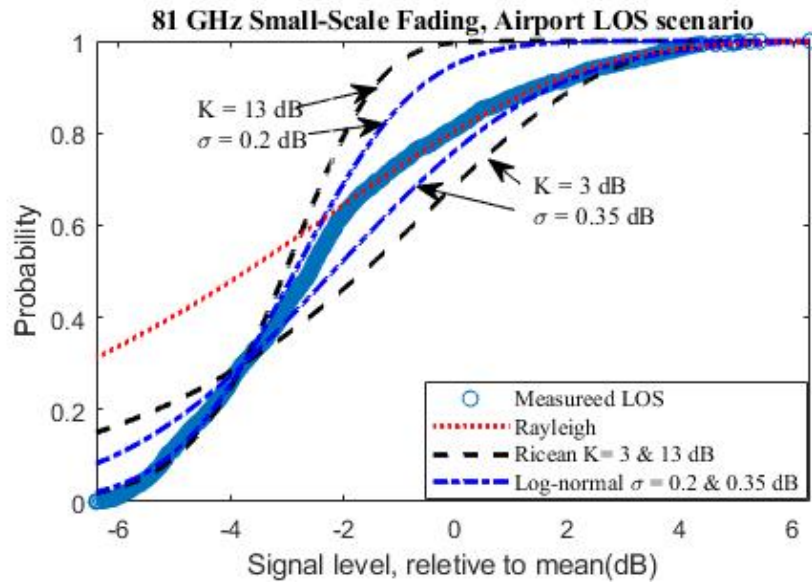
Figure 4.6: CDF of the measured 81 GHz small-scale fading of the received signal for the omnidirectional RX antenna pattern in the Airport LOS environment
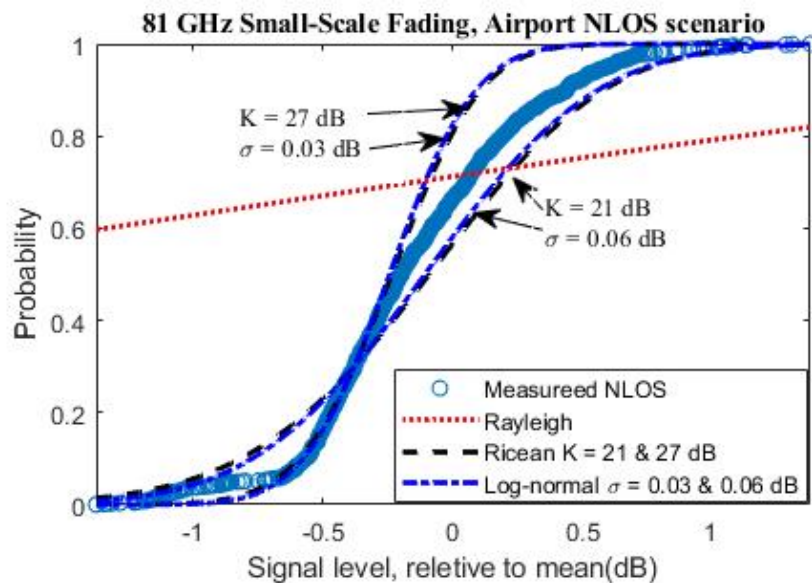
Figure 4.7: CDF of the measured 81 GHz small-scale fading of the received signal for the omnidirectional RX antenna pattern in the Airport NLOS environment
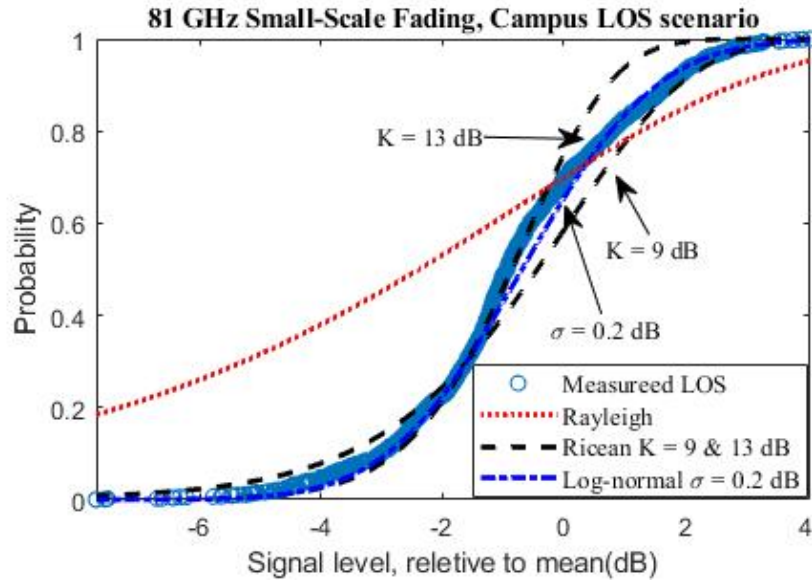
Figure 4.8: CDF of the measured 81 GHz small-scale fading of the received signal for the omnidirectional RX antenna pattern in the campus LOS environment

respectively. It also shows that the CDF curve is log-normally distributed bounded by $\sigma = 0.2$ dB and $\sigma = 0.35$ dB for the LOS condition, and $\sigma = 0.03$ dB and $\sigma = 0.06$ dB for the NLOS scenario . The Rayleigh distribution underestimates the measured data in both scenarios.

Moreover, the 81 GHz small-scale fading in the indoor LOS environment for the omnidirectional model is shown in Fig. 4.8. Similarly, the LOS data fits both with the Ricean and log-normal distribution in the indoor 81 GHz channel. Again, Rayleigh distribution fits the measured LOS data poorly.

4.7   Angular Power Profile

Angular characterization of multipath propagation is critical for a mmWave system that relies on high gain steerable antennas. An angular power profile is used to de-

scribe and characterize the spatial characteristics of multipath as a function of angle. While conducting the measurements, a unique angular power profile was obtained as the RX location changes for each LOS and NLOS scenario. Figs. 4.9 shows the angular power profiles at LOS and NLOS locations in an outdoor airport environment for the 73 and 81 GHz channel, respectively. The red circle indicates the -25 dBm reference line. The main lobe is pointed to TX for each LOS location at both frequencies, which results in LOS dominate path from the transmitter to the receiver.

As indicated in Figs. 4.9 , the stronger path is coming from the reflection of the terminal building in the NLOS scenarios at both bands. A weaker lobe appears in the direction of the TX location, which is most likely due to the scattering effects of the signal caused by nearby obstacles in the environment. This indicates that the mmWave channel will rely on beamforming and multipath caused by reflection and scattering. It can be seen that 73 GHz has a wider main lobe for the LOS location 2 in comparison to the 81 GHz band. Besides, 81 GHz main lobe power relative to average power over all directions is higher than that of the 73 GHz channel in the NLOS scenarios, which we expect.

4.8   Summary and Conclusion

This chapter presents small-scale fading and angular profile measurements at 73 and 81 GHz performed in the indoor LOS and NLOS environments at the Boise Airport. Besides, small-scale indoor measurements were conducted in a campus environment. The omnidirectional small-scale fading statistics are shown to be best characterized by a Ricean and log-normal distribution in all cases at both bands. The data fit well with the Ricean distribution in almost all scenarios because the strong dominant path has appeared in the measurement scenario. For the NLOS measurements, we avoided
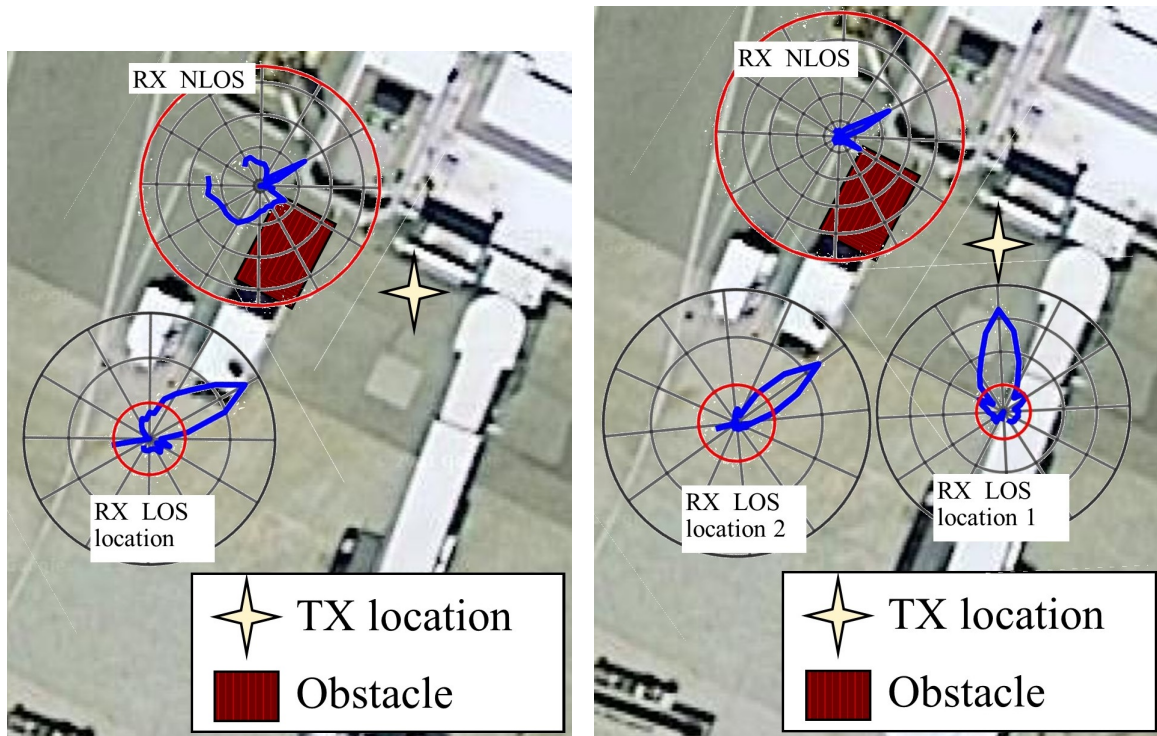
Figure 4.9: Angular power profile in Airport (a) 73 GHz showing LOS location 2 and NLOS location and (b) 81 GHz LOS location 1 and 2, and NLOS location.

the majority of the pathways owing to undetected signals. It can be seen that the Rayleigh distribution fades are deeper. This is most likely due to a strong LOS path in an indoor environment. The outdoor results reveal that the measured received multipath amplitude is bounded by the Ricean distribution of K-factor ranging from 3 to 14 dB, and log-normal distribution with $\sigma = 0.15$ dB and 0.37 dB for the 73 GHz LOS channel. However, the Rayleigh distribution underestimates the measured data poorly in all cases. Unique angular power profiles are obtained as the RX location changes for each LOS and NLOS scenario for the airport environment. These results indicate that 81 GHz main lobe power relative to average power overall directions are

higher than that of the 73 GHz channel in both LOS and NLOS scenarios.

CHAPTER 5:

PENETRATION, ATTENUATION AND REFLECTION LOSS MEASUREMENT CAMPAIGN

5.1   Introduction

We perform penetration and reflection measurements around the campus of Boise State University in three different settings for various bands—60, 73, and 81 GHz. In the first settings, we performed channel measurement campaigns at three buildings on the campus of BSU explained in Section 5.2. We measured the received signal strength of various indoor and outdoor building materials such as clear glass, tinted glass, wood, and drywall. In the second setting described in Section 5.3, we reported a collaborative work on building material attenuation in several mmWave frequency bands (28 GHz, 73 GHz, and 91 GHz). Our contribution was to report attenuation tests at 73 GHz in an indoor setting. In this section, we only present our contribution at 73 GHz. Standard building materials were ordered from the same retailer to have as close to identical materials as possible for comparison. Finally,in Section 5.4, we perform third settings of reflection measurement campaigns to test drywall and plywood materials in an indoor environment at mmWave frequencies—60, 73 and 81

GHz.

5.2 Penetration and Reflection Loss Measurements

During the spring of 2019, penetration and reflection measurements were performed. The hardware setup is depicted in Chapter 3 (Figs. 3.1 and 3.2). Reflection and penetration measurements for common building materials were conducted at three locations on campus at BSU in the city of Boise. These are 1) the Alumni and Friends Center, 2) Micron Engineering, and 3) Norco Building. Our measurements here pertain to the first-floor of the AFC. The overall layout of AFC can be found in Fig. 5.1, which resembles a typical office environment, with wood doors, tinted glass doors, and tiled/carpeted floors. There are several conference and ballrooms on both sides of the hallway. The door is made of solid-core fire-rated wood.

The second set of measurements was performed at the Norco Building, which exhibits a similar setting to an office environment with metallic doors, clear glass walls, and drywall. Measurements were made at three locations of several materials, i.e., clear glass, tinted glass, drywall, and metal doors. Our last measurement campaign was performed on the first floor of the MEC building. The floor has a long hallway with several laboratories and seminar rooms. The walls are made of sheetrock over metal studs, the ceiling tiles are made of a fiberboard material, and the ground is comprised of concrete.

5.2.1 Measurement Methodology

For both 73 and 81 GHz penetration loss measurements, the TX and RX were first separated by a certain separation distance. The distance, 4 m, was selected in free-space
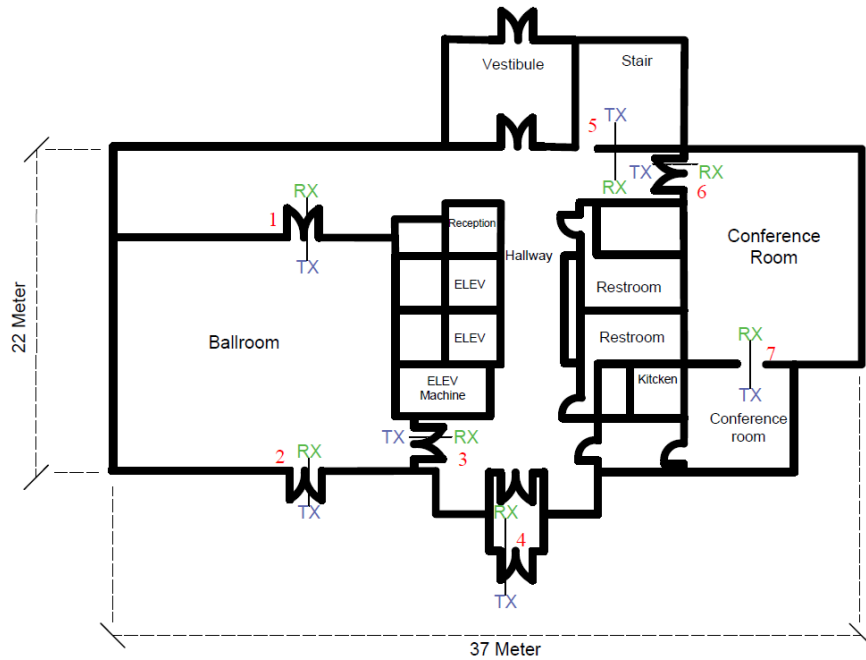
Figure 5.1: Floor plan of the 1st floor of Alumni and Friends Center, with TX and RX locations. Note that the doors were closed during measurements.

to provide a far-field reference path loss at the locations of measurement campaigns, as explained in the prior subsection. Then, the TX and RX were moved to be on each side of a test material while still keeping the same separation distance. Both TX and RX have placed 2 m away from the test material. The height of both TX and RX antennas was set at 1.5 m from the ground level. At each location, we approximately aligned the TX and RX antenna in boresights. We captured five power delay profiles at each TX-RX location, and the setup was kept fixed for each set of five repeated PDPs. Penetration loss was computed as the difference between average received power under a test material and the received power in unobstructed free-space with the same TX-RX separation. The relationship between propagation path loss and the

TX-RX separation distance is based on both the antenna heights and obstructions between the transmitter and receiver.

The path loss can be obtained from Eq 3.1 at a distance, d m [21] along with knowledge of transmit power for the penetration measurements. The penetration loss, L in dB can be obtained using (5.1).

$$L(dB) = PL^{unobs.}(d) - PL^{MUT}(d) \tag{5.1}$$

where,$PL^{MUT}(d)$ is the path loss for material under test which is denoted by MUT, and

$PL^{unobs.}(d)$ is the path loss in the unobstructed free-space distance.

For the reflection measurement, the transmitter and receiver were placed at d_1 m and d_2 away from the test material. Both TX and RX antennas were oriented at an incident angle, $\theta\circ$. The height of the antenna was identical to the setup of the penetration measurement campaigns. To determine the reflection coefficient, we measured the reflected power, $P_r(ref)$ under a test material [13, 21].

Along with the knowledge of LOS power and reflected power measurements, we obtained the magnitude of reflection coefficient from (5.2) [13, 21]

$$\mid \Gamma \mid = \frac{(d_1 + d_2)\sqrt{P_r(ref)}}{(d_{LOS})\sqrt{P_r(LOS)}}, \tag{5.2}$$

where, $P_r(LOS)$ is the received power in a line-of-sight scenario,

$P_r(ref)$ is the reflected power received by the RX,

d_{LOS} are the distance between TX and RX antennas in LOS scenario,

Table 5.1: Averages penetration loss of the indoor building materials with standard variation at a distance, 4 m. σ is the standard deviation of the penetration loss over all locations of a same type of material

Average penetration loss of several indoor building materials						
Frequency	Material	Thickness,cm	Locations	No of location	Average penetration loss, dB	Standard deviation σ,dB
73 GHz	clear glass	0.6	AFC	1	2.66	0.02
		1.0	NB	2		
	wood door	4.6	AFC	3	7.57	2.1
		4.2	MEC	1		
81 GHz	clear glass	0.6	AFC	1	3.18	0.56
		1.0	NB	2		
	wood door	4.6	AFC	3	9.05	2.4
		4.2	MEC	1		

Table 5.2: Comparison of reflectivity for different building materials at 73 and 81 GHz.

Frequency	Environment	Locations	Material	Angle, (∘)	Reflection Coefficient, ($\mid \Gamma_{\parallel} \mid$)
73 GHz	Outdoor	AFC	tinted glass	45	0.497
	indoor	AFC	wood	25	0.268
			clear glass	45	0.272
			wall	45	0.327
81 GHz	outdoor	AFC	tinted glass	45	0.620
	indoor	AFC	wood	25	0.313
			clear glass	45	0.287
			wall	45	0.395

d_1 and d_2 are the distance from Tx to the material and from Rx to the material.

5.2.2   Result Analysis

We made penetration measurements of a single material at several typical indoor environments to determine average penetration loss and standard deviation. Table 5.1 represents a summary of the average penetration losses of common indoor building materials at 73 GHz and 81 GHz. The standard deviation of penetration loss for all the locations of each indoor material is also provided in Table 5.1. The same types of materials were tested in at least two locations to characterize the effect of penetration loss with the thickness and formation of the material. At both 73 GHz

and 81 GHz mmWave channels, the penetration loss was obtained larger for the wood doors when we compared to the clear glass walls. At 73 GHz, the average penetration loss was measured to be 7.57 dB in the case of the wooden door. The thickness of the wood doors was measured, ranging in width from 4.2 to 4.6 cm, and the doors were constructed using two layers of solid wood cores. The average penetration loss for the wooden door at 81 GHz is increased to 9.05 dB, which was around 2 dB more attenuation than what was observed at 73 GHz because the penetration depends not only on the thickness and formation of the material but also on the carrier frequency.

Table 5.2 presents the reflection coefficients for common indoor and outdoor building materials. As indicated in Table 5.2, outdoor building materials had larger reflection coefficients in comparison to the indoor building materials at both bands. For example, at the 73 GHz channel, the tinted glass had reflection coefficients of 0.496.The lowest value was obtained for the clear glass door at 0.272, which we expect. At 81 GHz, the outdoor tinted glass had the larger reflection coefficient of 0.620. This means a large portion of the signal is reflected back, and a few portion signals could penetrate through the tinted glass. It is clear that indoor-to-outdoor penetration will be quite difficult at the high frequency, whereas signals at high frequencies can easily propagate in the indoor environment. This indicates that high-frequency reuse will be recommended between indoor and outdoor mmWave networks, which minimizes the interference.

5.3   Attenuation of Different Building Materials

In this section, we report on attenuation measurements of several typical building materials in three potential mmWave bands. The work is collaboration work on attenuation measurements conducted by three universities—University of South Car-

olina, Boise State University, and North Carolina State University, at 28, 73, and 91 GHz, respectively. In this chapter, we present building material attenuation measurement at 73 GHz. Using directional antennas, we took multiple measurements at multiple locations using narrow-band and wide-band signals and averaged out residual small-scale fading effects. Materials include clear glass, drywall (plasterboard), plywood, acoustic ceiling tile, and cinder blocks. Specific attenuations range from approximately 0.5 dB/cm for ceiling tile at 28 GHz to about 19 dB/cm for clear glass at 91 GHz.

5.3.1 Hardware Setup

The setup for building material attenuation is close to the setup, which is presented in Chapter 3, with different antenna combinations. In this setup, we did not require to use linear rail.

At the transmitter, AWG generated a Radar chirp signal at a 4 GHz with 500 MHz bandwidth. The IF signal was connected into an up-converter, with a LO at 38.5 GHz to upconvert to a 73 GHz signal. The RF signal was transmitted through a BPF and PA. Then finally, the output of PA was connected to a horn antenna. At the receiver, a band-pass rectangular waveguide filter was used at the RX to capture the signal. Afterward, a low noise amplifier, a downconverter, and a local-oscillator were employed for receiving the transmitted IF signal at 4 GHz. After mixing down, the received signal was fed to the scope, where PDP was measured using Keysight 89600 VSA software. We generated a radar chirp and a CW signal for the wideband and narrowband measurements, respectively. A wideband signal correlation time-domain channel sounding approach was employed for the wideband measurements. Table 5.3 shows the hardware specification we used for the 73 GHz attenuation measurement.

Table 5.3: Hardware Specifications for 73GHz Measurement Attenuation Measurement

Center Frequency, GHz	73
Wave Length, mm	4.1
Wideband Signal	Radar Chirp
Bandwidth(MHz)	500
Narrowband Signal	CW
TX Antenna	Rectangular Horn Antenna
TX Antenna Gain, dBi	12
Antenna Polarization	V-V
TX antenna 3dB Beamwidth in E the plane	45
TX antenna 3dB Beamwidth in H the plane	43
TX Antenna Diameter, A,cm	1.08
TX Antenna far-field for dmax,cm	5.6
Projection Diameter, D for dmax,cm	24.8
RX Antenna	WR-12 Waveguide

5.3.2 Measurement Procedure

We made some simple geometric calculations before starting measurements to guarantee that the primary lobe antenna projection on the material did not exceed the material dimensions. Otherwise diffracted and strong multipath components can reach the receiver and degrade material attenuation measurement accuracy. Building materials such as, plywood, acoustic ceiling, clear glass, drywall, and cinder blocks are used for the measurement. To minimize the variation from materials, three universities purchased the same brand from the same vendor across the US. The materials and their dimensions are listed in Table 5.4.

Fig. 5.2 shows the projection dimension for the antenna, where projection diameter is D,

$$D = 2d * tan(\alpha) \tag{5.3}$$

where,

α is half antenna beamwidth and

d is the separation between antenna and the material.

The guard projections width $g = r/2$, where r is the radius of the projection area or $r = D/2$. The dimension of the materials is big enough to cover the projection area of the main lobe of the antenna. All the materials in this work were chosen with greater dimensions than the projection and the guard annulus. Fig. 5.3 shows the testing setup for clear glass measurement. Note that during the actual measurement, a smaller dimension antenna was used for TX, and a waveguide was used for RX to meet the far-field region limitation. TX and RX antennas were placed at far-field distances where far-field is,

$$d > 2A^2/\lambda \qquad (5.4)$$

where d is the distance between TX-RX,

λ is the wavelength, and

A is the horn antenna aperture dimension.

We select TX-RX separations of d_1, d_2, and d_3 as 20, 25, 30 cm. At each location, TX and RX antennas are placed to face each other and perpendicular to the material. Having multiple locations minimizes error from antenna misalignment and material inhomogeneity.Fig. 5.4 shows TX and RX antenna placement during measurements. Building materials attenuation L can be estimated by Eq. 5.1.

5.3.3   Data Analysis

Table 5.5 presents a summary of average attenuation and standard deviation of measured building materials at 28, 73, and 91 GHz for wideband measurements.The standard deviations of attenuation across all the locations of each material are also
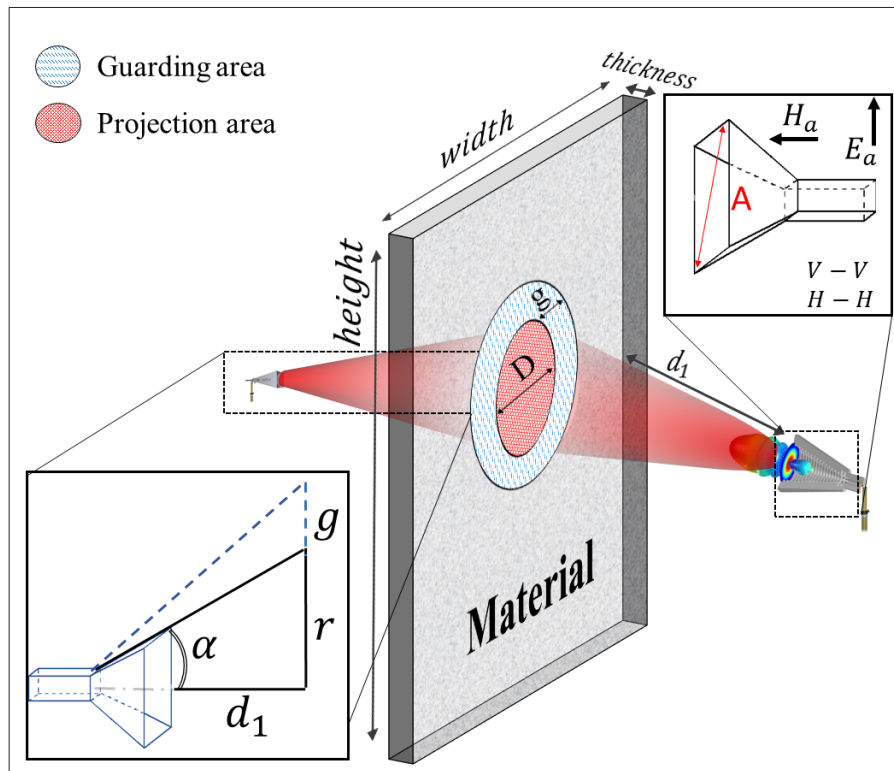
Figure 5.2: **Geometry for determining projection area and material dimensions with antenna dimension**

Table 5.4: Material List

Material	Manufacturer	Dimension
Plywood	Plytanium 15/32 CAT PS1-09, Pine 4-ply	$121.9cm \times 243.8cm$
Acoustic	Armstrong Acoustic Panel Ceiling Tiles	$121.9cm \times 60.9cm$
Clear Glass	Gardner Glass Products Panel	$76.2cm \times 91.4cm$
Drywall	ToughRock Fireguard Drywall Panel	$121.9cm \times 243.8cm$
Concrete block	Standard Core Concrete Block	$20cm \times 20cm \times 40.6cm$

Figure 5.3: Measurement picture for glass, with RX on the left and TX on the right. In the measurement a smaller dimension antenna was used for TX and waveguide was used for RX.

Figure 5.4: Measurement diagram, top view, with material in the middle, RX locations on the left, and TX locations on the right.

provided as well as total material attenuation in dB. As presented in Table 5.5, the clear glass has the highest attenuation among all standard materials at 73 and 91 GHz.

Table 5.5: Average specific attenuation with standard deviation at 28 GHz (NCSU), 73 GHz (BSU) and 91 GHz (USC) for wide band measurements. Cinder block attenuation at 91 and 73 GHz is only narrow band result due to large attenuation

Frequency	Material	Thickness, mm	Mean attenuation, dB/cm	Standard deviation, σ dB/cm
91 GHz	clear glass	1.8	18.79	6.39
	plywood	11.2	11.76	4.2
	drywall	13.1	1.97	1.26
	cinder block	195	2.13	0.22
	acoustic ceiling tiles	11.3	1.15	1.13
73 GHz	clear glass	1.8	9.07	0.55
	plywood	11.2	6.10	1.49
	drywall	13.1	1.4	0.46
	cinder block	195	2.0	0.07
	acoustic ceiling tiles	11.3	0.77	0.20
28 GHz	clear glass	1.8	4.38	0.18
	plywood	11.2	5.09	1.28
	drywall	13.1	0.94	0.23
	cinder block	195	1.03	0.18
	acoustic ceiling tiles	11.3	0.44	0.06
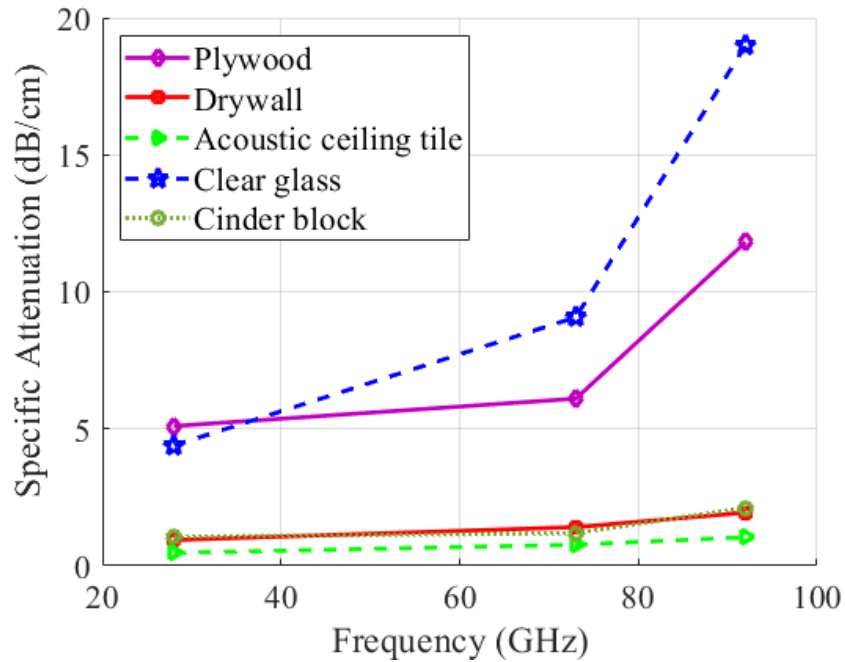
Figure 5.5: Average attenuation versus frequency at 28, 73, 91 GHz for all test materials

For example, the largest average specific attenuation of clear glass was measured to be 18.79 dB/cm and 9.07 dB/cm for the 91 and 73 GHz frequencies, respectively. The lowest values of specific attenuation were found for the acoustic ceiling panels and were 1.15 and 0.77 dB/cm at 91 and 73 GHz, respectively. For the 91 GHz and 73 GHz frequency bands, the largest and smallest standard deviations were found for clear glass and acoustic ceiling tiles, respectively. For 28 GHz, the largest standard deviation was measured as 1.28 dB/cm for plywood, and the lowest was obtained as 0.06 dB/cm for acoustic ceiling tile. Total attenuation in dB for each material is defined as the average attenuation over the thickness of that material. As expected, cinder blocks had the greatest attenuation in all three bands over the thickness. Note that at both 91 and 73 GHz, the attenuation for the cinder blocks was so large that we were unable to obtain wideband measurement results.

As noted, wideband measurement results were obtained via a frequency modulated signal (chirp) sweeping across the bandwidth, with the receiver using either a matched filter or heterodyne detector [7]. The wideband signals can also show any attenuation variation within the bandwidth. Wideband and narrowband measurement results (at 73 and 91 GHz) show a very close agreement: we have determined that the small difference is attributable to the out-of-band energy of the wideband signal that was not fully accounted for in our systems. Detailed figures showing attenuation can be found in Appendix D.

Fig. 5.5 presents average specific attenuation for all the materials in one plot. We observe that clear glass has the largest average specific attenuation, and acoustic ceiling tile has the smallest average specific attenuation.
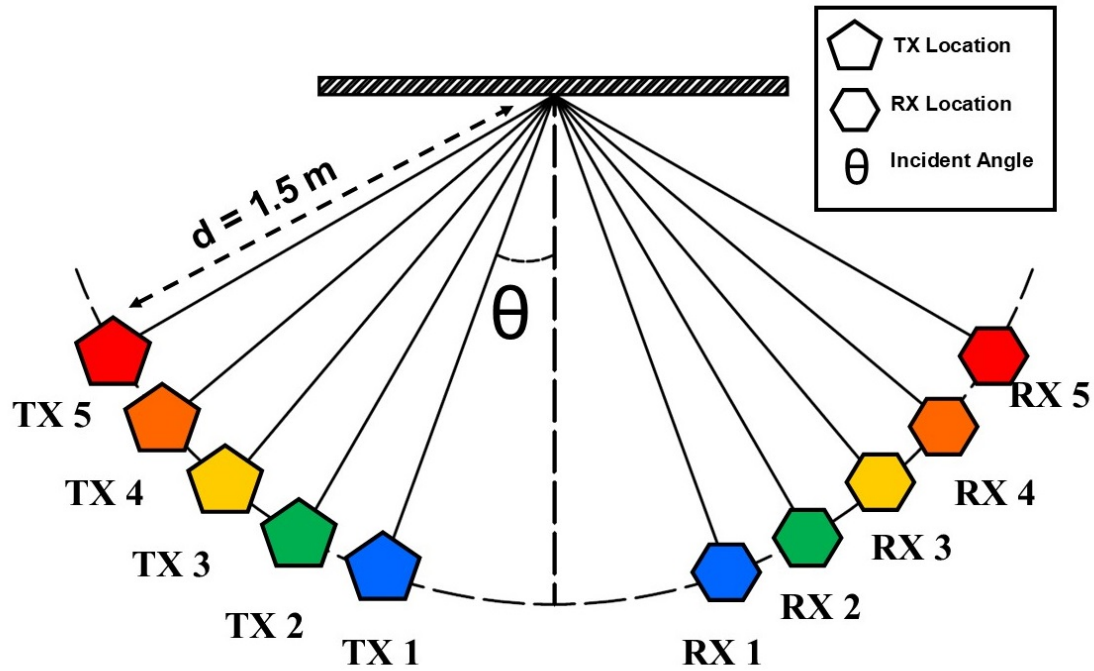
Figure 5.6: Reflection measurement procedure

5.4   Reflection loss Measurements

This section presents indoor reflection characteristics of common building materials at millimeter-wave frequencies. These channel properties are carefully studied at $60, 73$, and 81 GHz using a narrow-band signal with directional horn antennas. The TX and RX antennas were placed in the far-field region of both TX and RX antennas by 5.4, with distances to the materials set at 1.5 m. This guarantees that propagation takes place in the far-field (*geq* Fraunhofer distance). For the reflected power measurements, several incident angles of θ_i ($20°, 30°, 40°, 50°$ and $60°$) were chosen to measure reflected power off drywall and plywood at three mmWave channels —$60, 73$, and 81 GHz. Fig. 5.6 shows the TX and RX locations with different

angles during measurements. The received power was measured in five steps in the order of half-wavelength to avoid small-scale effects.
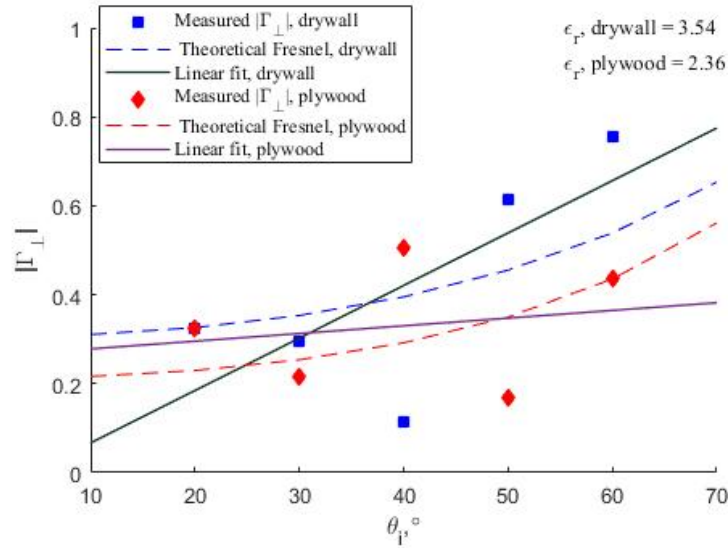
Figure 5.7: Measured magnitude of reflection coefficients, $| \Gamma_\perp |$ of drywall and plywood at 60 GHz

5.4.1   Reflection Measurement Results

The Fresnel reflection coefficient $|\Gamma_\perp|$ where the E-field is perpendicular to the plane of the incidence is presented by

$$| \Gamma_\perp | = \frac{| E_r |}{| E_i |} = \frac{\cos\theta_i + \sqrt{\epsilon_r - \sin\theta_i^2}}{\cos\theta_i - \sqrt{\epsilon_r - \sin\theta_i^2}}, \tag{5.5}$$

where, θ_i is the incident angle.

Based on the measured data in eq 5.2, the magnitude of the reflection coefficient, $| \Gamma |$, can be determined. Using Fresnel eq. 5.5, we estimated permittivity, ϵ_r of drywall and plywood using minimum mean squared error (MSE) at 60, 73 and 81 GHz bands.
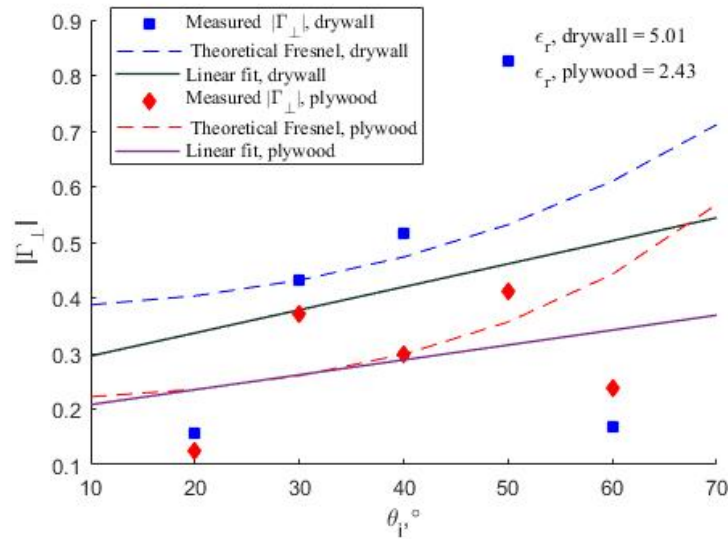
Figure 5.8: Measured magnitude of reflection coefficients, $|\Gamma_\perp|$ of drywall and plywood at 73 GHz
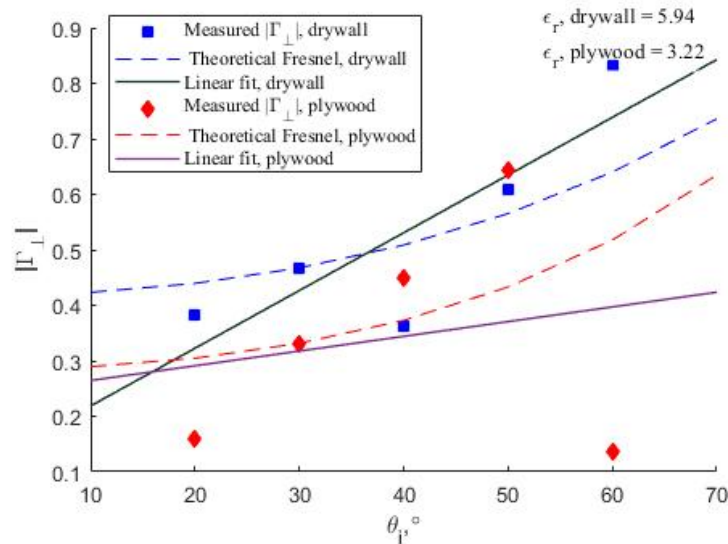
Figure 5.9: Measured magnitude of reflection coefficients, $|\Gamma_\perp|$ of drywall and plywood at 81 GHz,

Figs. 5.7, 5.8 and 5.9 show linear fit of the measured data, and the theoretical Fresnel curve through MSE estimation for drywall and plywood at three frequencies.

Table 5.6: Measured magnitude of reflection coefficients, $\mid \Gamma_\perp \mid$ and estimated estimated permittivity, ϵ_r of drywall and plywood at 60, 73, and 81 GHz

Frequency	Material	Incident Angle	$\mid \Gamma_\perp \mid$	ϵ_r
60	Drywall	20	0.326	3.54
		30	0.294	
		40	0.113	
		50	0.614	
		60	0.756	
	Plywood	20	0.325	2.36
		30	0.217	
		40	0.505	
		50	0.169	
		60	0.436	
73	Drywall	20	0.158	5.01
		30	0.432	
		40	0.516	
		50	0.826	
		60	0.169	
	Plywood	20	0.124	2.43
		30	0.371	
		40	0.299	
		50	0.410	
		60	0.239	
81	Drywall	20	0.38	5.94
		30	0.47	
		40	0.36	
		50	0.61	
		60	0.83	
	Plywood	20	0.16	3.22
		30	0.34	
		40	0.45	
		50	0.64	
		60	0.14	

The blue square and red pentagon points indicate the magnitude of the reflection coefficient at different incident angles for drywall and plywood, respectively. The

dashed and solid lines represent the theoretical Fresnel curve and linear fit for these two materials. We estimated permittivity, ϵ_r 3.54 and 2.36 for drywall and plywood, respectively at 60 GHz. It's worth noting that drywall has a higher projected permittivity than plywood, which is to be expected. At the 73 GHz channel, we found these values at 5.01 and 2.43, respectively. From Table 5.6, results also show that estimated permittivity, ϵ_r is smaller at lower frequencies and reflection coefficients, $|\Gamma_\perp|$ are stronger at higher frequencies. At 81 GHz, the range of $|\Gamma_\perp|$ varies from 0.38 to 0.83 with impinging direction (i.e., to the surface of drywall) for 20° to 60°, respectively. At all bands, plywood has a smaller reflection coefficient than drywall because of the dielectric property of this material.

5.5   Summary and Conclusion

We performed three measurement campaigns on our campus for various settings. In the first setting, The penetration was measured for various indoor and outdoor building materials such as clear glass, tinted glass, wood, metal, and drywall. We conducted channel measurement campaigns at three buildings on the BSU campus. The standard deviation examined among measurements of the indoor building materials at various locations were as large as 2.4 dB for the wooden door at 81GHz channel, and the lowest standard deviation was obtained to be 0.56 dB through the clear glass wall for the same frequency. Results suggest that electromagnetic waves can penetrate through glass walls or wooden doors reasonably well. Moreover, the outdoor building materials had a larger penetration loss at 73 GHz in comparison to the indoor building materials. This is most likely due to the thickness and formation of outdoor materials, which cause more attenuation and higher reflection than indoor materials. These results also indicate that high-frequency reuse is needed between

indoor and outdoor networks.

In the second setting, we reported on building material attenuation in three different mmWave frequency bands (28 GHz, 73 GHz, and 91 GHz). Standard building materials were ordered from the same retailer to have as close to identical materials as possible for comparison. These materials were clear glass, cinder blocks, plywood, drywall, and acoustic ceiling tiles. The measurement distances were calculated to ensure minimal signal distortion from other objects in the measurement environment, i.e., we strove to minimize effects from reflections, diffraction, and multi-path components. Nine measurement locations were used for both narrowband and wideband signals to reduce the effects of misalignment error and material inhomogeneity. Data was presented to show the range of measured variation caused by these effects. The largest specific attenuation at 91 GHz and 73 GHz was for clear glass, with values 18.79 and 9.07 dB/cm, respectively, and 5.09 dB/cm for plywood at 28 GHz. The smallest specific attenuation in all three bands was for acoustic ceiling tiles.

In the third setting, we perform reflection measurements in an indoor environment at mmWave frequencies—60, 73 and 81 GHz. Results indicate that estimated permittivity, ϵ_r is observed to be smaller at lower frequencies and reflection coefficients, $\mid \Gamma_\perp \mid$ are observed stronger at higher frequencies. At 60 GHz, the range of $\mid \Gamma_\perp \mid$ changes from 0.33 to 0.76 with impinging direction (i.e., to the surface of drywall) for $20°$ to $60°$, respectively, and has a trend towards increasing with frequencies.

CHAPTER 6:

CONCLUSION AND FUTURE WORK

This chapter addresses the implications and an overview of the results from each of the dissertation's preceding chapters. We also explain the future work directions of this dissertation here.

6.1 Summary and Conclusion

In this dissertation, we focus on channel measurements at three mmWave bands —60, 73, and 81 GHz that were conducted at Boise State University and the Boise Airport. Our measurement data will provide the wireless research community with unique data on channel models for these high-frequency bands in airport environments. We performed several path loss measurements at different high-frequency bands. Moreover, we collected data for the small-scale fading models at the Boise Airport and Boise State University. We have developed outdoor and indoor setups for reflection and penetration measurement of several building materials at these mmWave bands in a campus environment.

In Chapter 3, two large-scale path loss models are presented based on indoor and outdoor channel measurements at three mmWave bands —60, 73, and 81 GHz. The line-of-sight and non-line-of-sight millimeter-wave propagation measurement experiments were conducted *uniquely* in the indoor and outdoor environments at the Boise

Airport. The path loss exponents estimated by the CI are quite similar to those determined by the free-space path loss model, but the FI gives a superior match to the measurement data. These results also show that the indoor airport environment is uniquely different from other indoor settings due to its large and open nature. Also, the result shows that the standard deviation(σ) is higher at the airport indoor environment than the outdoor environment due to more obstacles appearing indoors, which creates a more reflective environment.

We present omnidirectional small-scale fading and angular power profile measurements and analysis at millimeter-wave frequency bands in Chapter 4. More than 825 power delay profiles were measured at each 73 and 81 GHz channel in an airport and campus environment. We carry out small-scale omnidirectional models and angular power profiles for both line-of-sight and non-line-of-sight environments. We collected various angular combinations of PDPs by controlling the beam directions of the transmitter and receiver antennas using a gimbal. Besides, a linear track was employed at each receiver to move the antenna in half-wavelength increments. Measured data indicate that small-scale fading of received signal amplitudes follow a Ricean and a log-normal distribution in the outdoor airport LOS and NLOS scenarios at 73 and 81 GHz bands. Results reveal that the cumulative distribution function curve is a Ricean distribution with K-factor ranging from $3 - 13$ dB, and $21 - 27$ dB and a log-normal distribution bounded by $\sigma = 0.2$ dB and $\sigma = 0.35$ dB for the LOS 81 GHz outdoor channel. The data fit well with the Ricean distribution in almost all scenarios because the strong dominant path has appeared in the measurement scenario. It can be seen that the Rayleigh distribution fades are deeper. This is most likely due to a strong LOS path in an indoor environment. Similar results can be seen at each band

for the indoor campus environment. In both LOS and NLOS scenarios, the angular power profile results show that main lobe power is higher at 81 GHz channel than 73 GHz channel in all directions, as expected.

In Chapter 5, we present three measurement campaigns in our campus at various bands —28, 73, 81 and 91 GHz. In the first setting, we performed channel measurement campaigns at three buildings on the campus of BSU. We tested various indoor and outdoor building materials such as clear glass, tinted glass, wood, and drywall. At both frequencies —73 and 81 GHz, average penetration loss was examined from 2 to 9 dB for the indoor materials. These results suggest that this high-frequency signal can penetrate through glass walls or wooden doors reasonably well. Moreover, the outdoor building materials had a larger reflection compared to the indoor building materials in both bands. This is most likely due to the thickness and formation of outdoor materials. Moreover, we reported our collaborative work on building material attenuation in three different mmWave frequency bands (28 GHz (NCSU), 73 GHz, and 91 GHz (USC). We tested the attenuation of clear glass, cinder blocks, plywood, drywall, and acoustic ceiling tiles. The largest specific attenuation at 91 GHz and 73 GHz was for clear glass, with values 18.79 and 9.07 dB/cm, respectively. In the third measurement campaign, we conducted reflection measurements in a lab environment at three mmWave frequencies—60, 73, and 81 GHz. These channel properties are carefully studied using a narrow-band signal with directional horn antennas. We measured the reflection coefficients at these high frequencies with varying incident angles to the surface of a material. Results indicate that estimated permittivity, ϵ_r is observed to be larger at higher frequencies.

6.2   Future Work

The research accomplished in this dissertation can open new research directions explained below:

In Chapter 3, we carry out two large-scale fading models, e.g., CI and FI path loss models based upon the measurement data. Other indoor and outdoor models can be utilized. Some path loss models, such as the multi-frequency alpha beta gamma model and multi-frequency CI model with a frequency-weighted path loss exponent, can be used to estimate the channel parameters. The ABG model aims to model large-scale path loss as a function of frequency and distance, while the CIF model seeks to capture the amount of linear frequency dependence of path loss about the weighted average of all frequencies.

Chapter 4 presents small-scale fading at the high-frequency bands. The CDF of measured received signal amplitude is compared only with three distributions: Rayleigh, Ricean, and log-normal distribution, but Airport LOS data does not fit well. In this case, Weibull distribution can be considered to be best fitted with the measured data.

In Chapter 5, materials for the penetration loss measurements are very limited to clear glass, tinted glass, drywall, etc. More standard materials can be added for future work. Polytetrafluoroethylene (PTFE) material can be used to help distinguish material inhomogeneity from misalignment error.

REFERENCES

[1] Spatial channel model for multiple input multiple output (MIMO) simulations. *3rd Generation Partnership Project, Sophia Antipolis Cedex*, France, TR 25.996, Sep. 2003.

[2] C. R. Anderson and T. S. Rappaport. In-building wideband partition loss measurements at 2.5 and 60 GHz. 3(3):922–928, May 2004.

[3] Andrea Goldsmith. *Wireless communications*. Cambridge university press, 2005.

[4] Katsuyuki Haneda, Jan Jarvelainen, Aki Karttunen, Mikko Kyro, and Jyri Putkonen. Indoor short-range radio propagation measurements at 60 and 70 GHz. *European Conference on Antennas and Propagation (EuCAP)*, pages 634--638, April 2014.

[5] Christopher J Hansen. Wigig: Multi-gigabit wireless communications in the 60 GHz band. *IEEE Wireless Comm.*, 18(6):6–7, 2011.

[6] Alexander H Henderson, Christopher J Durkin, and Gregory D Durgin. Finding the right small-scale fading distribution for a measured indoor 2.4 GHz channel. In *2008 IEEE Antennas and Propagation Society International Symposium*, pages 1–4. IEEE, 2008.

[7] N. Hosseini and D. W. Matolak. Wide band channel characterization for low

altitude unmanned aerial system communication using software defined radios. In *2018 Integrated Communications, Navigation, Surveillance Conf. (ICNS)*, pages 2C2–1–2C2–9, April 2018.

[8] M. Khatun, H. Mehrpouyan, and D. Matolak. 60 GHz millimeter-wave pathloss measurements in Boise Airport. *in Proc. IEEE Glob. Conf. on Signal and Inform. Process.*, pages 1276–1280, 2018.

[9] Mahfuza Khatun, Changyu Guo, Letizia Moro, David Matolak, and Hani Mehrpouyan. Millimeter-Wave Path Loss at 73 GHz in Indoor and Outdoor Airport Environments. *in Proc. IEEE Veh. Technol. Conf.*, pages 1–5, Sept. 2019.

[10] Pekka Kyosti. Winner II channel models. *Eur. Commission,Brussels*, Belgium, IST-WINNER, Tech. Rep. D1.1.2.

[11] Mikko Kyro, Veli-Matti Kolmonen, and Pertti Vainikainen. Experimental propagation channel characterization of mmwave radio links in urban scenarios. 11:865–868, Jul. 2012.

[12] Mikko Kyrö, Sylvain Ranvier, Veli-Matti Kolmonen, Katsuyuki Haneda, and Pertti Vainikainen. Long range wideband channel measurements at 81–86 GHz frequency range. In *IEEE Proceed. Conf. on Antennas and Propag.*, pages 1–5, 2010.

[13] Orlando Landron, Martin J Feuerstein, and Theodore S Rappaport. In situ microwave reflection coefficient measurements for smooth and rough exterior wall surfaces. In *IEEE 43rd Veh. Technol. Conf.*, pages 77–80, 1993.

[14] Y. C. Lee, S. Oh, H. C. Lee, C. Woo Byeon, S. W. Park, I. Lee, J. Lim, J. Lee, and B. Cho. Measurements of window penetration loss and building entry loss from 3.5 to 24 GHz. In *2019 13th European Conf. on Antennas and Propag. (EuCAP)*, pages 1–4, March 2019.

[15] George R MacCartney, Mathew K Samimi, and Theodore S Rappaport. Omnidirectional path loss models in New York City at 28 GHz and 73 GHz. In *IEEE Int. Symposium*, pages 227–231. IEEE, 2014.

[16] George R MacCartney, Junhong Zhang, Shuai Nie, and Theodore S Rappaport. Path loss models for 5G millimeter wave propagation channels in urban microcells. In *IEEE Glob. Comm. Conf.*, pages 3948–3953, 2013.

[17] Andreas F Molisch, Larry J Greenstein, and Mansoor Shafi. Propagation issues for cognitive radio. *Proc. IEEE*, 97(5):787–804, 2009.

[18] Juho Poutanen, Jussi Salmi, Katsuyuki Haneda, Veli-Matti Kolmonen, and Pertti Vainikainen. Angular and shadowing characteristics of dense multipath components in indoor radio channels. *IEEE Transactions on Antennas and Propagation*, 59(1):245–253, April 2011.

[19] Sundeep Rangan, Theodore S Rappaport, and Elza Erkip. Millimeter-wave cellular wireless networks: Potentials and challenges. *IEEE Proceed.*, 102(3):366–385, 2014.

[20] T. S. Rappaport, S. Sun, R. Mayzus, H. Zhao, Y. Azar, K. Wang, G. N. Wong, J. K. Schulz, M. Samimi, and F. Gutierrez. Millimeter wave mobile communications for 5G cellular: It will work! *IEEE Access*, 1:335–349, 2013.

[21] Theodore S Rappaport et al. *Wireless communications: principles and practice.* 2nd ed. Upper Saddle River, NJ, USA: Prentice-Hall, 2002.

[22] Theodore S Rappaport, Felix Gutierrez, Eshar Ben-Dor, James N Murdock, Yi-jun Qiao, and Jonathan I Tamir. Broadband millimeter-wave propagation measurements and models using adaptive-beam antennas for outdoor urban cellular communications. 61(4):1850–1859, 2012.

[23] Theodore S Rappaport, Robert W Heath Jr, Robert C Daniels, and James N Murdock. *Millimeter wave wireless communications.* Englewood Cliffs, NJ, USA: Prentice Hall, 2015.

[24] Theodore S Rappaport, George R MacCartney, Mathew K Samimi, and Shu Sun. Wideband millimeter-wave propagation measurements and channel models for future wireless communication system design. 63(9):3029–3056, 2015.

[25] Theodore S Rappaport, Scott Y Seidel, and Koichiro Takamizawa. Statistical channel impulse response models for factory and open plan building radio communicate system design. *IEEE transactions on communications*, 39(5):794–807, 1991.

[26] J. Ryan, G. R. MacCartney, and T. S. Rappaport. Indoor office wideband penetration loss measurements at 73 GHz. In *in Proc. IEEE Int. Conf. Commun. Workshops*, pages 228–233, May 2017.

[27] Mathew K Samimi, George R MacCartney, Shu Sun, and Theodore S Rappaport. 28 GHz millimeter-wave ultrawideband small-scale fading models in

wireless channels. In *2016 IEEE 83rd Vehicular Technology Conference (VTC Spring)*, pages 1–6. IEEE, 2016.

[28] Mathew K Samimi and Theodore S Rappaport. 3-D statistical channel model for millimeter-wave outdoor mobile broadband communications. In *IEEE Int. Conf. on Commun.*, pages 2430–2436, June. 2015.

[29] Pal Fan Man Smulders and Air Gnuuy Wagemans. Wide-band measurements of mm-wave indoor radio channels. *Third IEEE International Symposium on Personal, Indoor and Mobile Radio Communications (PIMRC)*, pages 329—-333, October 1992.

[30] Pal Fan Man Smulders and Air Gnuuy Wagemans. Wideband indoor radio propagation measurements at 58 GHz. *Electronics Letters*, 28(13):1270—-1272, June 1992.

[31] Pal Fan Man Smulders and Air Gnuuy Wagemans. Frequency-domain measurement of the millimeter wave indoor radio channel. *IEEE Transactions on Instrumentation and Measurement*, 44(6):1017—1022, December 1995.

[32] Shu Sun, Hangsong Yan, George R MacCartney, and Theodore S Rappaport. Millimeter wave small-scale spatial statistics in an urban microcell scenario. In *2017 IEEE International Conference on Communications (ICC)*, pages 1–7. IEEE, 2017.

[33] Yunchou Xing, Ojas Kanhere, Shihao Ju, and Theodore S. Rappaport. Indoor Wireless Channel Properties at Millimeter Wave and Sub-Terahertz Frequencies. *in Proc. IEEE Global Commun. Conf.*, pages 1–5, Dec. 2019.

[34] Hao Xu, Vikas Kukshya, and Theodore S Rappaport. Spatial and temporal characterization of 60 GHz indoor channels. In *IEEE Veh. Technol. Conf., Fall 2000*, volume 1, pages 6–13, 2000.

[35] Hao Xu, Vikas Kukshya, and Theodore S Rappaport. Spatial and temporal characteristics of 60-GHz indoor channels. *IEEE J. Sel. Areas Commun.*, 20(3):620–630, 2002.

[36] Hang Zhao, Rimma Mayzus, Shu Sun, Mathew Samimi, Jocelyn K Schulz, Yaniv Azar, Kevin Wang, George N Wong, Felix Gutierrez, and Theodore S Rappaport. 28 GHz millimeter wave cellular communication measurements for reflection and penetration loss in and around buildings in New York City. In *Proc. IEEE Int. Conf. Commun.*, pages 5163–5167, Jun. 2013.

APPENDIX A:

LINEAR TRACK SYSTEM

This system contains four parts. Fuyu FL80 Linear rail, ST-M5045 stepper motor controller, AC-DC buck converter, and Arduino UNO microcontroller. Fig.A.1b shows the block diagram of the Linear rail system. The AC-DC buck converter output 24 V DC voltage to power the Linear rail motor and the motor controller. The Arduino is programmed to send out pulses, with a push of a button on a breadboard, to the motor controller which drives the motor in linear rail.

The Arduino is programmed to send out 640 pulses with a single push of a button, speed of motion, and the movement distance per button push, can be varied by modifying the pulse. With the current setting on the motor driver, each pulse moves the linear rail 0.032mm. Motor driver settings can be changed for more resolution options.
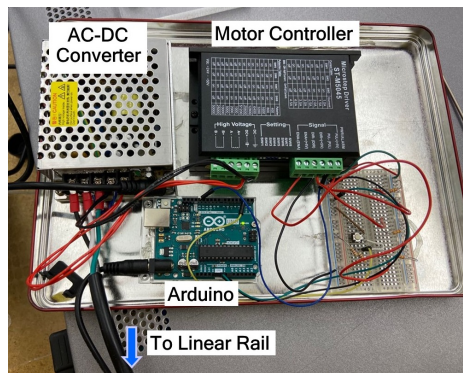
(a) Linear Rail Control module setup
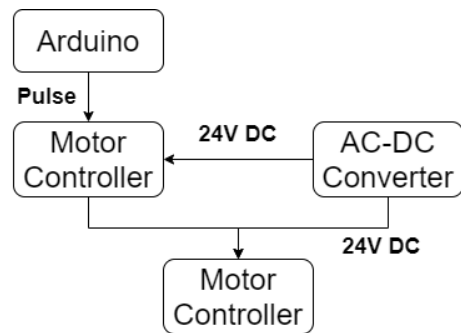
(b) Linear Rail System Block Diagram

Figure A.1: Linear Rail Module
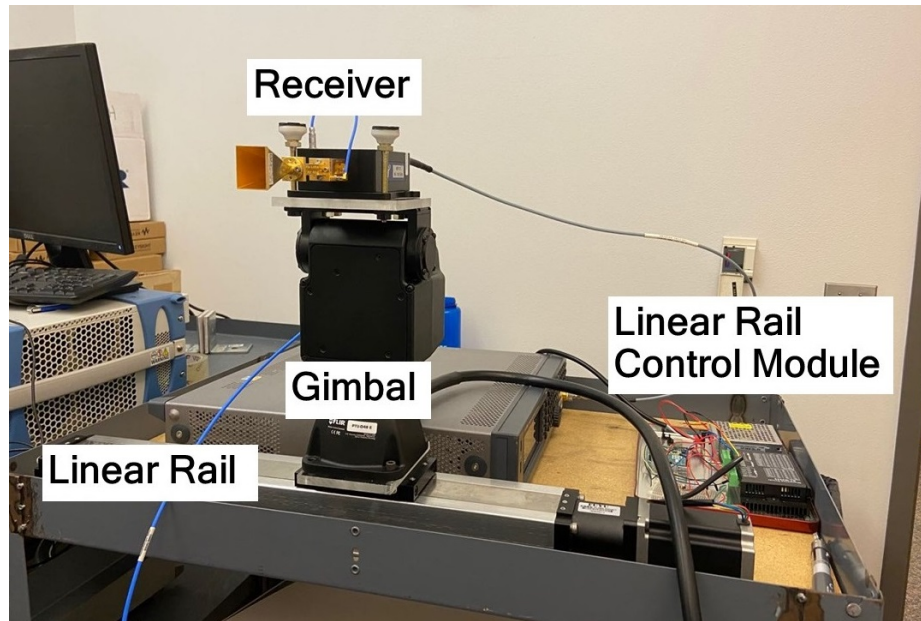
Figure A.2: Linear rail with Gimbal and RX mounted on cart

APPENDIX B:

PAN-TILT UNIT

The Pan-Tilt Unit is controlled by laptops. Each PTU is connected to a laptop with SR-232 to usb cable. The control code is written in MatLab, integrated with data recording SCPI code. Two laptops are connected through UTP on WLAN. Fig. B.1 shows the block diagram of the PTU control system.
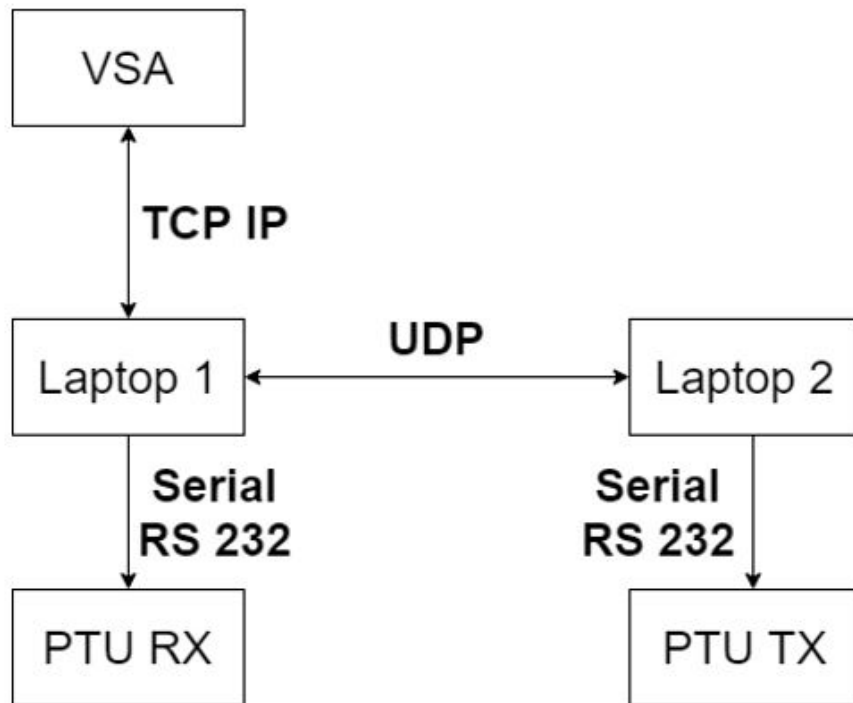
Figure B.1: PTU Control System Diagram

The control code in MatLab contains PTU control and VSA data recording functionality. Fig. B.2 shows the control flow of the MatLab script. The RX control script starts first and then the TX control script. The TX script will control the PTU move to a designated angle then send a done message to the UDP buffer. When the RX control script receives the done message, it moves the PTU then captures data from VSA software. After the data capture finishes, a done message is sent to the

UPD buffer as TX is waiting.
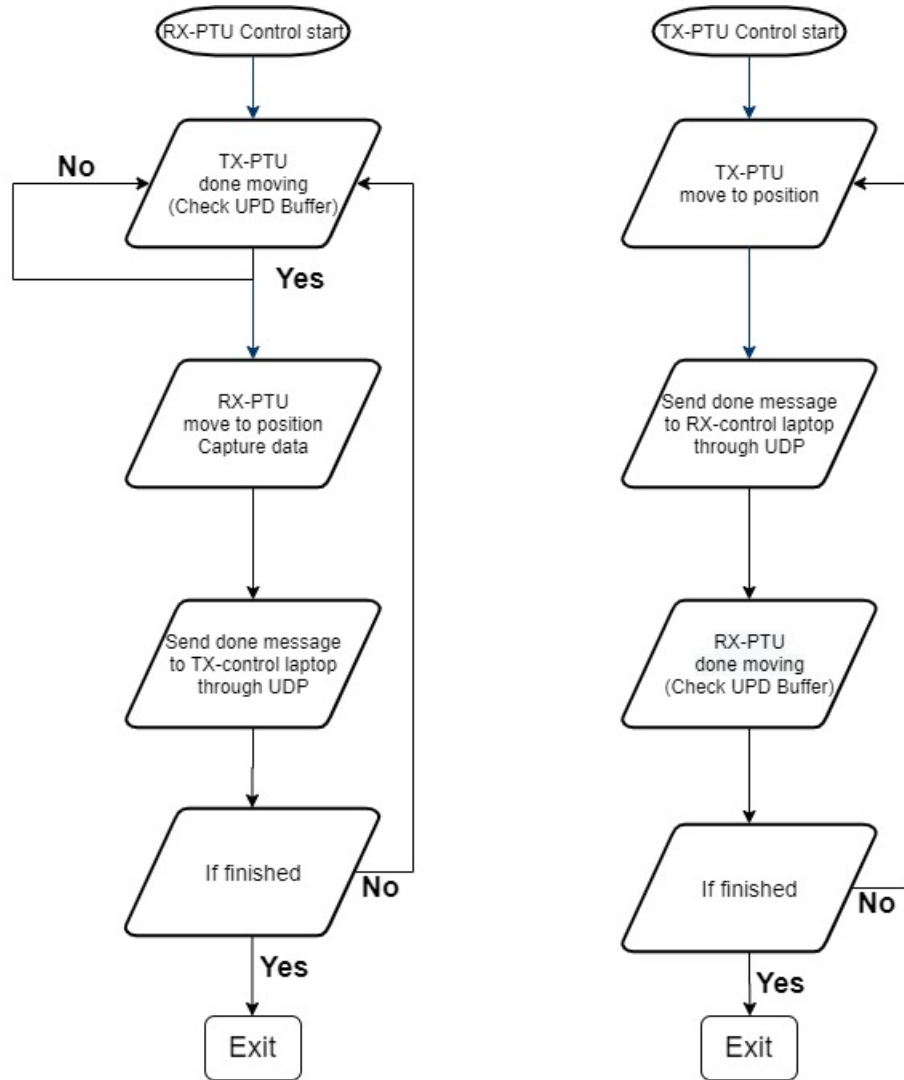
Figure B.2: PTU Control flow

APPENDIX C:

FIGURES OF FOR PATH LOSS AND

PENETRATION MEASUREMENT
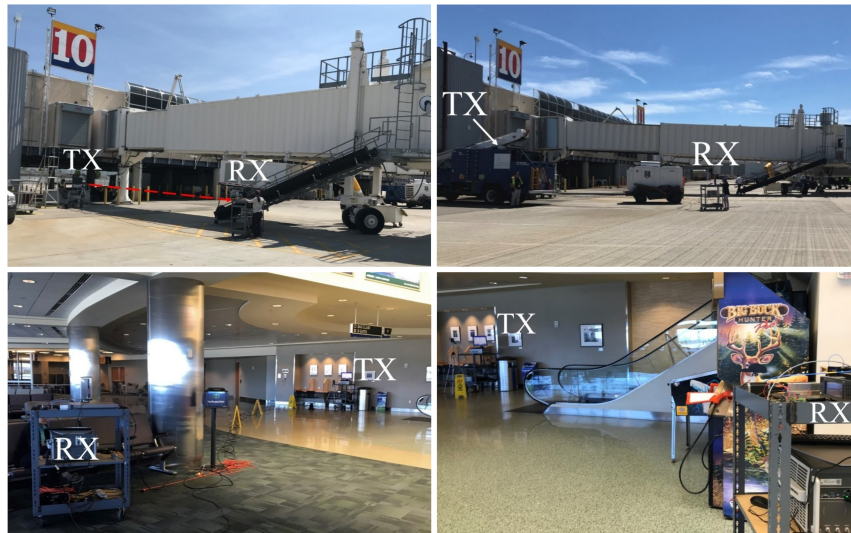
Figure C.1: Images of path loss measurements at Boise Airport for outdoor environments in LOS (top left), NLOS (top right), and for indoor environment in LOS (bottom left), NLOS (bottom right) scenarios.
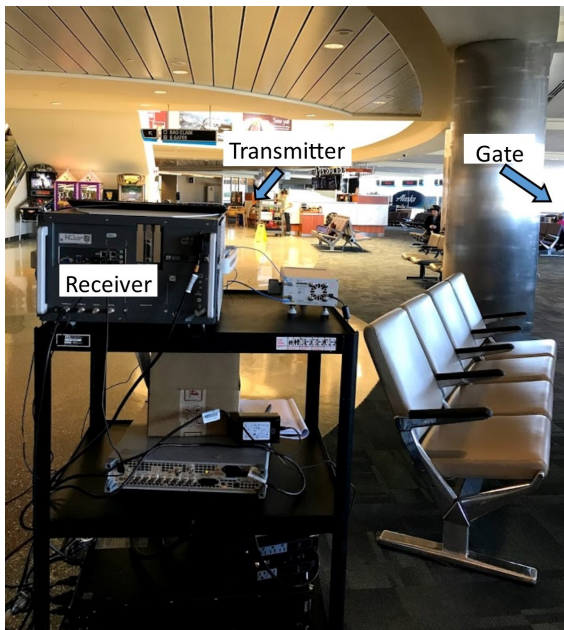
(a) Airport gate area

(b) Airport baggage claim area

Figure C.2: 60 GHz channel measurement conducted in airport gate and baggage claim areas

Figure C.3: Pictures of the 73 **GHz penetration measurement for indoor clear glass wall (left) at NB and outdoor metal door (right) at MEC. Both TX and RX antennas were bore-sighted on a material indicated by a red box.**

Figure C.4: Pictures of the 81 **GHz reflection measurement for outdoor tinted glass (left) and indoor wooden door (right) at AFC. Both TX and RX antennas were bore-sighted on a material with an incident angle indicated by a red box.**

APPENDIX D:

ADDITIONAL FIGURES FOR MATERIALS ATTENUATION MEASUREMENT
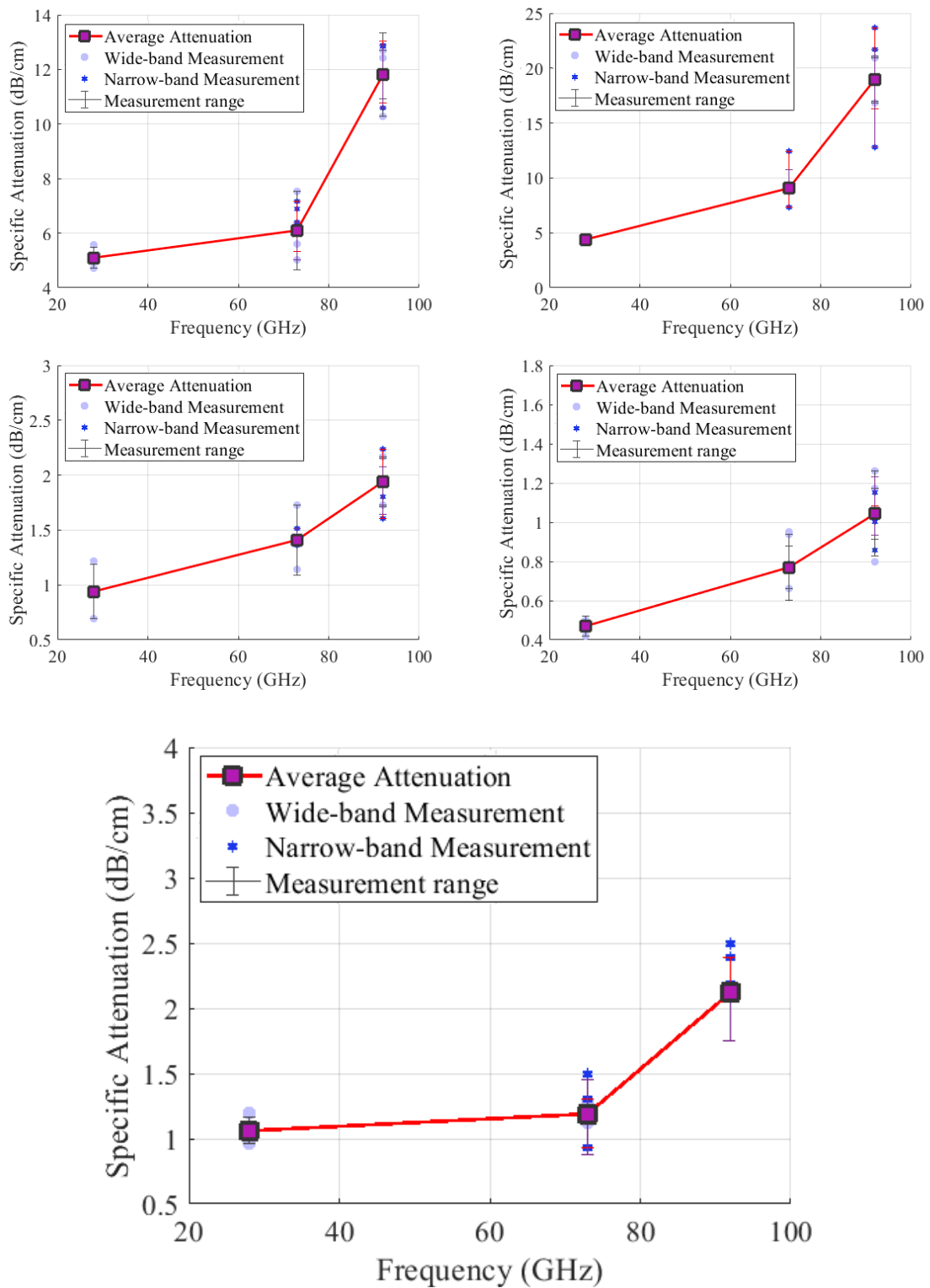
Figure D.1: Specific Attenuation versus Frequency for different materials. top left: plywood, top right: glass, middle left: drywall, middle right: concrete, bottom: ceiling tile